

NASA TECHNICAL
MEMORANDUM

NASA TM X-53538

November 14, 1966

NASA TM X-53538

ON CROSS-BEAM MONITORING OF ATMOSPHERIC
WINDS AND TURBULENCE WITH TWO
ORBITING TELESCOPES

By F. R. Krause, S. S. Hu, and A. J. Montgomery
Aero-Astroynamics Laboratory

FACILITY FORM NO.	N67 14913 (ACCESSION NUMBER)	_____ (THRU)
	93 (PAGES)	_____ (CODE)
	TMX-53538 (NASA CR OR TMX OR AD NUMBER)	13 (CATEGORY)

NASA

*George C. Marshall
Space Flight Center,
Huntsville, Alabama*

GPO PRICE \$ _____

CFSTI PRICE(S) \$ _____

Hard copy (HC) 3.00

Microfiche (MF) 1.30

TECHNICAL MEMORANDUM X-53538

ON CROSSED-BEAM MONITORING OF ATMOSPHERIC WINDS AND
TURBULENCE WITH TWO ORBITING TELESCOPES

By

F. R. Krause, S. S. Hu, and A. J. Montgomery

George C. Marshall Space Flight Center

Huntsville, Alabama

ABSTRACT

This report documents the phase A feasibility study on the MSFC inflight experiment No. 23, entitled "Crossed-Beam Arrangements for Remote Sensing Missions." The crossed-beam test arrangement employs triangulation of two collimated beams of radiation for the remote sensing of the space and time variations of thermodynamic state variables such as tracer concentrations. The generation, convection and decay of trace constituents (aerosols, ozone, and water vapor) will modulate the mean radiative power, which is put into the telescope's field of view by an extended radiation background such as scattered sunlight or thermal emission. The associated fluctuations of radiative power are then correlated to retrieve local information at the beam intersection from the integrated optical signals. The potential of crossed-beam test arrangement is illustrated by discussing analytically the measurement of horizontal wind profiles. It is conceivable to conduct crossed-beam missions with two astronomical telescopes (ATM) which are mounted on a single spacecraft in such a way that they point towards the earth.

N67-14913

NASA - GEORGE C. MARSHALL SPACE FLIGHT CENTER

Technical Memorandum X-53538

November 14, 1966

ON CROSSED-BEAM MONITORING OF ATMOSPHERIC WINDS AND
TURBULENCE WITH TWO ORBITING TELESCOPES

By

F. R. Krause, S. S. Hu*, and A. J. Montgomery**

*This work was partially performed under contract NAS8-20082
with Northrop Space Laboratories.

**This work was partially performed under contract NAS8-20107
with IIT Research Institute.

AEROPHYSICS DIVISION
AERO-ASTRODYNAMICS LABORATORY
RESEARCH AND DEVELOPMENT OPERATIONS

ACKNOWLEDGEMENTS

The reference material on meteorological application and natural backgrounds of radiation was partially collected and analyzed by Mr. S. V. Paranjape and Dr. J. G. La France from NSL under Dr. Hu's supervision.

The authors would like to acknowledge the participation of Mr. J. B. Stephens, R-AERO-AM, Mr. R. E. Cummings, R-AERO-T, and Dr. W. O. Davis, IITRI, in the discussions which were essential for the preparation of this paper. Constructive criticisms and comments from Prof. E. Reiter, C.S.U., Mr. J. Scoggins and W. Vaughan, R-AERO-Y have been most helpful. The authors would like to thank Mrs. Evelyn E. Carter, R-AERO-PR, for preparation of the figures, and Mrs. S. Hightower, R-AERO-R, for editing the final manuscript.

TABLE OF CONTENTS

	<u>Page</u>
I. INTRODUCTION.....	1
II. DEFINITION OF SYMBOLS.....	3
III. REVIEW OF THE CROSSED-BEAM METHOD.....	5
1. Optical Signals from a Single Beam.....	5
2. Retrieval of Local Information.....	7
3. Measurable Turbulence Parameters.....	11
4. Experimental Status.....	14
IV. CONCEIVABLE IN-FLIGHT EXPERIMENTS.....	16
V. EXPECTED OPTICAL SIGNALS.....	18
1. Mean Radiance of Extended Natural Sources.....	18
2. Meteorological Power Modulations.....	25
3. Detector Noise.....	27
VI. THEORY OF CROSSED-BEAM SCANNING.....	29
1. Geometry of Scanning Beams.....	30
2. Length Averages of Frozen Patterns.....	33
3. Interpretation of Two-Beam Product Mean Values.....	36
4. Measurement of Altitude Profiles.....	40
VII. STEP-BY-STEP SIMULATION OF IN-FLIGHT EXPERIMENTS.....	41
1. Test Arrangements.....	42
2. Preliminary Specifications.....	42
3. First Generation Experiments.....	46
4. Second Generation Experiments.....	47
CONCLUSIONS.....	48
APPENDIX A. Approximation of Point Correlations in Locally Isotropic Fields.....	76

LIST OF ILLUSTRATIONS

<u>Figure</u>	<u>Title</u>	<u>Page</u>
1	Space Fixed Crossed Beam Test Arrangements.....	52
2	Remote Sensing of Local Changes in Radiative Power.....	53
3	Retrieval of Local Information.....	54
4	Optical Integration Over Correlation Areas (Disc).	55
5	Evaluation of Space Correlations.....	56
6	Evaluation of Time Correlations.....	57
7	Crossed Beam Correlation in a Subsonic Jet.....	58
8	Time Correlations from Crossed Beam and Hot Wire Measurements.....	59
9	Velocity Profiles from Hot Wire and Crossed Beam Methods.....	60
10	Crossed Beam Test Arrangements for Horizontal Wind Measurements.....	61
11	Crossed Beam Spectroscopy.....	62
12	Dependence of Scattered Solar Radiation on Latitude and Sun Elevation Angles.....	63
13	Emission Spectrum of Atmospheric Radiation Background For Two Altitudes (15).....	64
14	Spectral Radiance of the Sunlit Side of Earth as Observed from a Satellite.....	65
15	Atmospheric Modulation of a Laser Beam.....	66
16	Tracer and Air Density Distribution with Height...	67
17	Translation of a Rigid Crossed Beam Arrangement...	68

LIST OF ILLUSTRATIONS (Continued)

<u>Figure</u>	<u>Title</u>	<u>Page</u>
18	Points of Minimum Separation A_i and B_i Between Imaginary and Undelayed Beam.....	69
19	Group Velocity Measurement with Scanning Beams.	70
20	Estimate of Normalized Autocorrelation and Space Correlation Functions.....	71
21	Photo Detector Assembly for Sweeping Altitude Profiles.....	72
22	Telescope Motions for Crossed Beam Scanning....	73

ON CROSSED-BEAM MONITORING OF ATMOSPHERIC WINDS AND
TURBULENCE WITH TWO ORBITING TELESCOPES

SUMMARY

This report documents the phase A feasibility study on the MSFC inflight experiment No. 23, entitled "Crossed-Beam Arrangements for Remote Sensing Missions." The crossed-beam test arrangement employs triangulation of two collimated beams of radiation for the remote sensing of the space and time variations of thermodynamic state variables such as tracer concentrations. The generation, convection and decay of trace constituents (aerosols, ozone, and water vapor) will modulate the mean radiative power, which is put into the telescope's field of view by an extended radiation background such as scattered sunlight or thermal emission. The associated fluctuations of radiative power are then correlated to retrieve local information at the beam intersection from the integrated optical signals. The potential of crossed-beam test arrangement is illustrated by discussing analytically the measurement of horizontal wind profiles.

I. INTRODUCTION

Crossed-beam test arrangements of ground and orbiting detectors have been studied to determine whether the remote sensing of horizontal wind profiles and turbulence parameters is feasible. Two remote sensing devices are used to measure the space and time variations of local emission and extinction processes. The fluctuations of the two optical signals are combined in a cross-correlation analysis to retrieve the signals which are common to both beams out of atmospheric and instrument noise in a way known from signal processing and random vibration analysis. This combination of remote sensing and cross-correlation analysis has been called the "crossed-beam concept." Early versions were proposed independently by M. J. Fisher [1] for jet noise studies and M. Wolf [2] for airglow studies. These results showed that correlations from hot wire and crossed-beam observations in subsonic jets yield identical results for convection speeds [1] and that crossed-beam observations of the airglow altitude are in agreement with rocket observations [2]. Thus, the crossed-beam correlation method is theoretically sound, and it has been shown experimentally to provide results in agreement with more accepted methods.

In most remote sensing methods, the attenuation or emission of electromagnetic radiation is measured along the entire path from the source to the detector. To interpret the results of such an observation, some assumption is generally required. For example, in atmospheric studies, one might use the adiabatic or isothermal model atmosphere. Assumptions for dynamic studies are made concerning symmetry, expansion properties, and temperature. The important point is that, with single path observations, it is not generally possible to obtain spatially resolved measurements of the thermodynamic or flow properties without invoking such models.

In crossed-beam experiments, theoretical models need not be invoked. The spatial and temporal variation of turbulence and, hopefully, thermodynamic properties would be measured in sometimes inaccessible regions, where other methods are restricted to a mean value over the entire optical path or to a direct measurement in a single point. The potential applications of crossed-beam experiments, therefore, include almost every conceivable experiment in which the basic measurement requires monitoring space and time variations of atmospheric species and contaminants. This could include observations of low level and clear air turbulence, motion and distribution of air pollution from industrial wastes and rocket tests, evaporation over oceans, and ozone motion and distribution (which bears some relation to global weather patterns). It might also be possible to study the nature and motion of targets of opportunity such as storms, hurricanes, meteors, cometary dust, and noctilucent clouds.

The feasibility and potential of crossed-beam experiments in the lower atmosphere are illustrated by considering the operation which would be necessary to measure a horizontal wind profile up to altitudes of 30 km. In chapter III, the theory of space-fixed beam crossings is reviewed to indicate how repeated experiments with different beam separation distances provide for an accurate statistical description of the space and time variations in any random field which produces detectable fluctuations of radiative power. Chapter IV gives the ultimate objective of in-flight experiments with crossed beams. In chapter V scattering and reflection of sunlight, thermal radiation from the atmosphere or the earth and nonthermal emission in the atmosphere are introduced as extended natural sources of radiative power that need not be tracked. Measured modulations of laser light indicate that atmospheric fluctuations do produce detectable fluctuations, even under a clear sky, which are not obscured by receiver noise. The use of these natural sources then provides for extremely flexible test arrangements, which could sweep the entire altitude profile of horizontal winds with a single fly-by using orbital detectors or with a repeated scan, using ground detectors. A global sweep requires crossed-beam scanning, the theory of which is given in chapter VI. In chapter VII a series of fundamental ground

experiments is outlined which would ultimately simulate the sweep with orbiting detectors. Preliminary specifications are given for both ground and orbital detectors.

II. DEFINITION OF SYMBOLS

<u>Symbol</u>	<u>Definition</u>
α	beam inclination relative to the plane of the sweeping beam normal
β	inclination of intersection paths relative to beam front
b	baseline or distance between telescopes
B	bandwidths of data acquisition chain in cps
D	eddy diffusion coefficient for mass transport
E	eddy diffusion coefficient for momentum transport
e	charge of one electron
f	turbulence frequency
I	detected radiative power
$i = I - \bar{I}$	detectable power fluctuation or optical signal
$K = \frac{1}{I} \frac{\partial I}{\partial x}$	extinction or emission coefficients (simultaneous emission and extinction are to be excluded)
$k = K - \bar{K}$	fluctuations of extinction coefficient
$L_{x,y,z}$	integral scale of turbulence in x,y,z direction, respectively
N	number of desired altitude points
p	length coordinate along beam trajectory
P	path length considered in the averaging procedure
Q	quantum efficiency [electrons/photon]
$R_k(\vec{\xi}, \tau)_{\vec{x}, \lambda}$	$= \overline{k(\vec{x}, t, \lambda) k(\vec{x} + \vec{\xi}, t + \tau, \lambda)}$ two point product mean value

SymbolDefinition

ρ	density of air
$R(\vec{\xi}, \tau)_{\vec{x}, \lambda}$	$= \overline{i_y(t) i_z(t + \tau)}$ correlation of detected fluctuations ("two beam product mean value")
t	time
T	static temperature or integration time
U, V, W	velocity components in space-fixed frame
$W = \bar{W} + w$	vertical velocity component
x	horizontal length coordinate normal to both beams
y	horizontal length coordinate parallel to beam front
z	vertical coordinate
$\vec{x} = (x, y, z)$	point vector in space-fixed Cartesian frame
η, ζ	beam-fixed coordinates relative to the line of minimum beam separation
λ	optical wave length
$\Delta\lambda$	wave length interval set by the optical filter
$\lambda/\Delta\lambda$	spectroscopic resolution
ξ	minimum beam separation defining wave normal
$\vec{\xi} = (\xi, \eta, \zeta)$	point vector in coordinate system occupied by beam structure at time zero
\emptyset	$\frac{R(\xi, \tau)_{\vec{x}, \lambda}}{R(0, 0)_{\vec{x}, \lambda}}$ space time correlation coefficient
τ	time lag

Superscripts

\rightarrow	vector
-	ensemble, space and/or time average
$\langle \rangle$	time average for moving observer
-p	length average over intersection path

Subscripts

z,y or 1,2	line of sight in z,y direction
*	moving frame autocorrelation
C	group velocity component (convection of disturbances normal to beam front)
A,B	points of minimum beam separation

III. REVIEW OF THE CROSSED-BEAM METHOD

1. Optical Signals from A Single Beam

In a crossed-beam arrangement the local flow region of interest may be chosen by triangulation between two collimated beams and extends between the two points \vec{x} and $\vec{x} + (\xi, 0, 0)$ of minimum beam separation. A typical test arrangement for jet noise studies is shown in figure 1. The beam diameters (viewing angle) and orientation (azimuth and elevation) are set by a remote telescope. The collected radiative power is then filtered by a monochromator, which is set at the wave length λ and the resolution $\Delta\lambda$ as illustrated in figure 2. The remaining signal, I_d , is then monitored by a photodetector with a fast response such that the time history is not lost.

The remote sensing device will see any local emission or extinction process inside the beam. We choose to express the contributions to the radiative power ΔI , which originate in a beam element, Δx , by a generalized spectral extinction coefficient

$$K(\vec{x}, t, \lambda) = \frac{1}{I} \frac{\partial I}{\partial x} . \quad (1)$$

The word "generalized" indicates that emission processes are included. As long as either emission or extinction is locally dominant, the equations of radiative transfer show that the total signal, I , may be expressed in terms of a line integral over the extinction coefficient.

$$I_d(t, \lambda) = I_{\text{source}} \exp \left(- \int_{\text{source}}^{\text{detector}} K(\vec{x}, t, \lambda) dx \right) . \quad (2)$$

The fluctuation of this signal,

$$i = I_d - \bar{I}_d, \quad (3)$$

can be calculated by subtracting a mean value \bar{I} , which may be established by averaging over time and/or over repeated experiments. In case of ideal detectors, this fluctuation is related to the fluctuations of the extinction coefficient

$$k = K - \bar{K} \quad (4)$$

through the line integral of equation (2).

$$I_d = I_{\text{source}} e^{\int_{\text{source}}^{\text{detector}} (\bar{K} + k) dx}$$

$$= (\bar{I}_s + i_s) \exp \left(- \int_{\text{source}}^{\text{detector}} \bar{K} dx \right) \left\{ 1 - \int k dx + \frac{1}{2} \left(\int k dx \right)^2 + \dots \right\}. \quad (5)$$

It is now assumed that the integrated k fluctuations of the medium can be treated as small perturbations.

$$\left| \int_{\text{source}}^{\text{detector}} k(\vec{x}, t, \lambda) dx \right| \ll 1. \quad (6)$$

In this case the last equation can be rearranged to give the desired fluctuation:

$$i = I_d - \bar{I}_d = \frac{\bar{I}_d}{\bar{I}_s} i_{\text{source}} - \bar{I}_d \int_{\text{source}}^{\text{detector}} k(\vec{x}, t, \lambda) dx. \quad (7)$$

The first term gives the contribution of the light source noise, and the second accounts for the fluctuations of the medium. Detector noise has to be added for nonideal detection devices.

The small perturbation assumption is not very restrictive. The transmission

$$\int \bar{K} dx,$$

as well as the local values of the fluctuation k could be large. Only the fluctuation integral over several statistically independent parts has to be small enough to permit linearization.

2. Retrieval of Local Information

The way the beam correlation works to retrieve the local information at the region of minimum beam separation becomes clear by introducing the concept of a "correlation volume." This volume is defined in turbulence theory by an imaginary experiment with two-point observers, as illustrated in figure 3. We consider a special arrangement where the beams are aligned parallel to the y and x axis and cross in the space-fixed position \vec{x} . The first imaginary observer shall be attached to this position. The second observer monitors the k fluctuations at the variable position $\vec{x} + \vec{\xi}$, and the imaginary experiment now calls for multiplying and averaging the observed fluctuations. This gives a "two-point product mean value,"

$$R_k(\vec{\xi}, \tau, \lambda) = \overline{k(\vec{x}, t, \lambda) k(\vec{x} + \vec{\xi}, t + \tau, \lambda)}, \quad (8)$$

which is the basis of all analytical descriptions of random fields [5]. The random nature of a fluctuation field such as $k(\vec{x}, t, \lambda)$ is recognized by the fact that the two-point product mean value drops to zero over finite distances $|\vec{\xi}|$. This leads to the definition of the correlation volume. It is that volume surrounding a certain point \vec{x} , within which the two-point product mean value R_k remains finite. The average radius of this volume in the x -direction is used to define the integral length scale:

$$L_x = \frac{1}{2} \int_{-\infty}^{+\infty} \frac{\overline{k(x + \xi, y, z, t) k(\vec{x}, t)}}{k^2(\vec{x}, t)} d\xi. \quad (9)$$

Similar expressions hold for the extensions $2L_y$ and $2L_z$ of the correlation volume in the y and z directions. In wind tunnels typical L values are between 1 mm and 10 cm. In the atmosphere they vary between 10 m and 1 km.

A crossed-beam experiment resembles the above imaginary experiments by performing exactly the same calculations. Only the local fluctuations of k are replaced with the fluctuations i of the detected signal, I. This leads to the "two-beam product mean value"

$$R(\xi, \tau, \lambda) = \overline{i_y(t, \lambda) i_z(t + \tau, \lambda)}. \quad (10)$$

The relation between two-beam product and two-point product mean values is now derived by splitting the detectable optical fluctuations i_y and i_z into three different components, as shown in figure 3.

$$i_y = i_{y1} + i_{y2} + i_{y3}.$$

The first component describes the contribution of the correlation volume

$$i_{yi} = \int_{\text{correlation volume}} k(x + \xi, y + \eta, z, t + \tau, \lambda) d\eta. \quad (11)$$

The second contribution accounts for the medium fluctuations outside the correlation volume; that is, for the flow noise,

$$i_{y2} = \int_{\text{source}}^{\text{detector}} k d\eta - i_{y1}. \quad (12)$$

The third contribution summarizes light source noise and detector noise.

$$i_{y3} = i_s \cdot \frac{\bar{I}_d}{\bar{I}_s} + \text{detector noise}. \quad (13)$$

The instantaneous product of the two optical signals may thus be written as the sum of nine other products,

$$i_y i_z = i_{y_1} i_{z_1} + i_{y_2} i_{z_2} + \dots + i_{y_3} i_{z_3}. \quad (14)$$

The last eight of these products have one noise component as a factor. Their instantaneous value will thus assume positive and negative values. If we average these products, their sum will decrease to zero with at least the inverse square root of integration time and/or number of experiments. The first product contains the fluctuations inside the correlation volume which are common to both lines of sight. The instantaneous product of these fluctuations is always positive, and its average value will thus approach a constant value with increasing integration time and/or number of experiments. This product will outweigh all others if we add long enough. In the limit of infinitely long summation, one should be able to retrieve almost infinitesimal contributions i_{y_1} and i_{z_1} .

$$R = \overline{i_z(t) i_y(t + \tau)} = \overline{i_{y_1} i_{z_1}} = R(\vec{\xi}, \tau, \lambda)_{\vec{x}} \quad (15)$$

Accordingly, the cross-correlation has pulled the correlated signals from the correlation volume out of the flow noise (i_{y_2}, i_{z_2}) and instrument noise (i_{y_3}, i_{z_3}). Substituting the line integrals for i_{y_1} and i_{z_1} , equation (11), inverting the order of integration and averaging, gives the following alternate form of the last equation:

$$R(\vec{\xi}, \tau, \lambda)_{\vec{x}} = \bar{i}_y \bar{i}_z \int \int_{\text{correlation volume}} \overline{k(x, y, z - \zeta, t, \lambda_1) k(x + \xi, y + \eta, z, t + \tau, \lambda_2)} d\eta d\zeta. \quad (16)$$

The crossed-beam method can do better than resolving only the correlation volume. This follows from a more detailed consideration of the optical integration. The above product of two line integrals can be transformed to an area integral,

$$R(\vec{\xi}, \tau, \lambda)_{\vec{x}} = \bar{i}_y \bar{i}_z \int \int_{\text{correlation "disc"}} R_k(\vec{\xi}, \tau, \lambda)_{\vec{x}} d\eta d\zeta, \quad (17)$$

if the fluctuations are locally homogeneous along one beam. The transformation is identical with the condition of statistical homogeneity, and its application leads to an integrand, where only the second point is variable.

$$\begin{aligned}
& \overline{k(x,y,z - \zeta, t, \lambda_1) k(x + \xi, y + \eta, z, t + \tau, \lambda_2)} = \\
& = \overline{k(x,y,z, t, \lambda_1) k(x + \xi, y + \eta, z + \zeta, t + \tau, \lambda_2)}. \quad (18)
\end{aligned}$$

The area integration is illustrated in figure 4. The integrand is equal to the two-point product mean value between two observers. The first observer is fixed to the upstream point \vec{x} of minimum beam separation. The second observer may be anywhere in a plane which is parallel to both beams and contains the second point $(x + \xi, y, z)$ of minimum beam separation. This plane will be called the beam front. The two-beam product mean value is thus identical with an optical integration over the beam front. Since along the beam normal no integration takes place, it is possible to resolve two-point product mean values inside the correlation volume by repeating the experiment for several beam separations, ξ .

The following analytical considerations, as well as M. J. Fisher's experiments [6], lead us to the conclusion that the area integrations are weighing the points close to the beam normal such that the normalized two-beam product mean value \emptyset closely approximates a two-point product mean value between the two points \vec{x} and $\vec{x} + (\xi, 0, 0)$ of minimum beam separation:

$$\emptyset(\xi, \tau, \lambda)_{\vec{x}} = \frac{R(\xi, \tau, \lambda)_{\vec{x}}}{R(0, 0, \lambda)_{\vec{x}}} \approx \frac{R_k(\xi, 0, 0, \tau, \lambda)}{R_k(0, 0, 0, 0, \lambda)} \frac{\bar{I}_y(\xi \neq 0)}{\bar{I}_y(\xi = 0)}. \quad (19)$$

The errors of this approximation are small in the two extreme cases of very small and very large lateral scales L_y and L_z . In case of very small lateral scales the weighting of points close to the wave normal is self-explanatory. In case of a large lateral scale, the fluctuations will be provided by an almost periodic wave of infinite extent, that is, in the limit by a plane acoustic wave. This follows from the well known property of Fourier transform pairs, which states that if the correlation is broad (large turbulence scale) then the spectrum (extension in wave numbers) will be narrow. However, in case of acoustical waves, a separation-of-variables assumption holds for separations in time and along the wave normal.

$$\overline{k(x,y,z,t) k(x + \xi, y + \eta, z + \zeta, t + \tau)} = \emptyset(\xi, \tau) \overline{k(x,y,z,t) k(x,y + \eta, z + \zeta, t)}. \quad (20)$$

Substituting the separation of variables into both (18) and (19), we find that these conditions are met identically.

For intermediately sized correlation volumes, the two-beam approximation of two-point product mean values, equa. (19), is not always valid. For locally isotropic turbulence which is closely approximated by atmospheric turbulence at the ground, the derivations given in the appendix show that the two-point product mean value should be directly proportional to the second derivative of the two-beam product mean value with respect to the separation distance:

$$\text{isotropic } R_k(\xi; \eta = 0; \zeta = 0; \tau)_{\vec{x}, \lambda} = \frac{1}{8\pi^3} \frac{\partial^2}{\partial \xi^2} R(\xi, \tau)_{\vec{x}, \lambda} . \quad (21)$$

For small separation distances, the function $R(\xi, \dots)$ can be approximated by a cosine curve, since $R(\xi, \dots)$ is an even function of ξ because of the isotropy. However, the second derivative of a cosine curve is directly proportional to the cosine curve itself and the proportionality factor drops out when normalizing as required by equation (19). For small separation distances and locally isotropic fields, equation (19) should thus be valid for correlation volumes of any size. For large separations, and anisotropic, inhomogeneous turbulence errors are to be expected. Fortunately, the experiments discussed in section III,4 indicate that the approximation of point measurements may still be good in many anisotropic and inhomogeneous fields of practical interest such as jet streams.

3. Measurable Turbulence Parameters

The crossed-beam method approximates two-point product mean values, and the two-beam product mean values can therefore be used to approximate all turbulence parameters which are commonly derived from two-point product mean values [8].

The local integral scale of turbulence is defined by averaging the area under the space correlation, $R(\xi, \tau = 0)$, and its graphical evaluation is illustrated on figure 5. This scale L_x is a measure for the extent of correlation volume along the beam normal. For mean value estimates as well as error discussions, we would also like to know the lateral integral scales L_y and L_z . These could be measured by rotating the lines of sight so that they can be separated parallel to the y and z directions.

Plotting the beam correlation coefficient against the time separation instead of the space separation (figure 6) allows group velocities to be read. For a given space separation, the correlation will reach a maximum at the time that the turbulent eddies need to travel from the upstream to the downstream beam. The time lag, τ_M , which is indicated by the maximum is therefore a direct measure of group velocities. A crossed-beam experiment is thus capable of measuring the component of the group velocity, which is normal to the beam front. In atmospheric applications, these components will be horizontal, since the beams are mostly parallel to a vertical plane.

A group velocity represents an average velocity of a disturbance [11]. It will in general differ from a mass average velocity. In spite of this fact, the name "bulk convection speed" is often used in turbulence investigations [8]. Later sections of this report will use the assumption that the group velocity of a crossed-beam experiment closely approximates a mass average velocity, i.e., a horizontal wind. The two velocities will be equal, if positive and negative amplitudes of the correlated signals i_{y1} , i_{z1} are equally likely, that is, if the first order probability density is symmetrical. Extreme cases of unsymmetrical or skewed first order probability densities occur in shear layers. Fortunately, the experiments shown in figure 8 indicate that the difference between group velocities and mass average velocities is not too great even in such extreme conditions. We therefore believe, that a crossed-beam system gives horizontal winds with sufficient accuracy to be of practical interest. In case of excitation problems, such as a rocket going through clear air turbulence, one needs to know the group velocities and not the mass average velocities.

The envelope to the individual temporal correlations (figure 6) is called the moving axis autocorrelation, since the associated two-point product mean values are those which would be seen by two observers moving with the group velocity [9]. The study of the envelope enables us thus to study the generation and decay of targets of opportunity such as shock waves and weather fronts independent from the convection processes. The decay of this correlation curve of 1/e of its original value is used to define the average "eddy" lifetime. The Fourier transform of this envelope would indicate the dominant frequencies which are felt by the moving observer, traveling with the target.

An observer traveling with the bulk convection speed will record almost the same transport phenomena [8] as the observer who travels along in a single fluid particle. The moving axis autocorrelation or envelope,

$$\phi^*(\tau_M) = \phi\left(\xi, \tau_M = \frac{\xi}{U_C}\right) = \frac{R(\xi, \tau_M)_{\vec{x}, \lambda} \bar{I}_y(\xi = 0)}{R(0, 0)_{\vec{x}, \lambda} \bar{I}_y(\xi \neq 0)}, \quad (22)$$

is the closest approximation of the Lagrangian autocorrelation functions which is accessible to direct or remote sensors. The moving axis time scale,

$$L_{\tau} = \int_0^{\infty} \phi^*(\tau_M) d\tau_M, \quad (23)$$

therefore closely approximates the Lagrangian time scale. This allows an important contribution to the experimental analysis of turbulent transport phenomena. The observed extinction coefficient fluctuations, k , are very often directly proportional to the fluctuations ρ'_{tr} in the tracer concentration which in turn indicate a turbulent mass flux, $\overline{\rho'_{tr} w}$ across horizontal planes. From the point of view of "turbulent diffusion," this mass flux should be directly proportional to the vertical gradient of the mean tracer concentration:

$$\overline{\rho'_{tr} w} \Big|_{\text{space-fixed}} = D \frac{\partial \bar{\rho}_{tr}}{\partial z}. \quad (24)$$

However, describing the diffusion process through the random walk of a single particle, we find that the eddy diffusion coefficient, D , is equal to the product between the mean square value of the vertical velocity fluctuations and the Lagrangian time scale [10].

$$D = \overline{w^2} \Big|_{\text{moving axis}} \cdot L_{\tau}. \quad (25)$$

Combining the last two equations leads to a direct relation between the moving axis time scale, L_{τ} , and the density gradient:

$$\frac{\partial \bar{\rho}_{tr}}{\partial z} = \frac{\overline{\rho'_{tr} w} \Big|_{\text{space-fixed}}}{\overline{w^2} \Big|_{\text{moving axis}}} \cdot \frac{1}{L_{\tau}}. \quad (26)$$

The concept of turbulent diffusion can be applied to momentum diffusion instead of mass diffusion. In this case, the turbulent flux is given by the apparent turbulent shear stress, $\rho \overline{uw}$, and the driving mean velocity gradient $\partial \bar{U} / \partial z$:

$$\rho \overline{uw} = \rho E \frac{\partial \bar{U}}{\partial z}. \quad (27)$$

If the eddy diffusivity, E , is approximately equal to the mass diffusion coefficient, D (turbulent Lewis number $E/D = 1$), equation (25) can still be used. Its substitution leads to an expression for the shear:

$$\frac{\partial \bar{U}}{\partial z} = \frac{\overline{uw} \Big|_{\text{space-fixed}}}{\overline{w^2} \Big|_{\text{moving axis}}} \frac{1}{L_\tau} \quad (28)$$

Experimental evidence suggests that one-point correlation coefficients between velocity components like the one shown on the right-hand side are rather insensitive to position on the turbulent field [8]. We might therefore expect that the shear is almost inversely proportional to the moving axis time scale. In subsonic jet shear layers, this has been demonstrated already through the hot-wire experiments of Davies and Fisher [7].

4. Experimental Status

The first crossed-beam experiments were designed to verify the approximation of two-point product mean values in very general fields of turbulence. The "imaginary" point probes were approximated by hot-wire probes. Although a small hot wire gives velocity fluctuations rather than extinction coefficient fluctuations, a comparison between hot wires and crossed-beam correlation coefficients should give identical results as long as we are interested only in the dynamical description of turbulence in terms of scales, the group velocities, and the spectra. The initial portion of an axisymmetric, free shear layer was chosen for the experiments since the turbulence is anisotropic and inhomogeneous and since group velocities, turbulence scales, and eddy lifetimes are well documented in the literature.

All measurements were taken in a subsonic ($M = 0.2$) air jet exhausting through a one-inch diameter nozzle into the atmosphere. Light extinction was achieved by spraying a small amount of liquid nitrogen into the settling chamber. This produces small water droplets in the exhaust flow which attenuate the crossed beams by scattering. Later, the nitrogen injection was replaced with water spray, which offers a better control of the tracer concentration.

A typical sample of optically measured two-beam product mean values is shown in figure 7. The beam intersection was adjusted to the center of the free shear layer three exit diameters downstream of the nozzle lip. The turbulent convection process is clearly indicated by the displaced maxima for finite beam separation. The envelope to these maxima falls to $1/e$ of its initial value for a time lag of 880 microseconds. This is in excellent agreement with the hot-wire data from which we estimate that the value of the eddy lifetime for our experimental conditions should be 920 microseconds.

Figure 8 shows the same experiment under different conditions. The initial intersection point of the beams was six diameters from the jet exit, (i.e., at $x/D = 6.0$) instead of at $x/D = 3.0$). Instead of using liquid nitrogen to generate a water droplet fog tracer, a small nozzle was mounted in the jet settling tank which sprayed water droplets into the flow to form the tracer fog. The curves appear to fall onto or close to an envelope as required. The moving axis autocorrelation curve has been obtained from the hot-wire data of Davies, et al., [7] and is shown as the dotted line superimposed on the measured cross correlation curve.

The spatial resolution of the crossed-beam method seems very encouraging, considering that the envelope from the hot-wire data exactly matches the individual curves from the crossed-beam method. For the moving frame, the optically measured autocorrelation agreed with the hot-wire curves, regardless of whether nitrogen or water spray was used as a tracer.

The optically measured results in figure 8 were only 0.2 inch apart. This is much smaller than the geometrical shear layer thickness ($\approx .8$ in) which is indicated by the hot-wire results. Thus, space-time correlations have been resolved inside a correlated volume by moving the intersection point.

The spatial resolution obtainable with crossed-beam test arrangements becomes more apparent by comparing optically measured group velocities with hot-wire group velocities. Our main results are summarized in figure 9. In the central and low speed portions of the shear layer ($\eta > 0$), the convection velocity determinations agree within experimental accuracy. For $\eta < 0$, however, the crossed-beam results tend to follow the mean velocity profile (U/U_0) rather than attain the constant maximum value observed for hot-wire data. The experiments of Davies [12] indicate that hot wires at the high velocity edge of a shear layer react to sound radiation from the shear layer center as well as to the convection of upstream turbulence. A low value of the hot-wire group velocity is therefore to be expected because of the convection of the sound sources which travel in the middle of the shear layer with lower velocity than the edge particles. Instruments other than the hot wire should give higher group velocities, as indicated by the crossed-beam method.

The optical group velocity measurements used tracers. Since then, we have succeeded in measuring convection speeds in supersonic jets without tracers. These tests used the density fluctuation of air to produce changes of radiative power in the ultraviolet absorption bands of oxygen (Schumann-Runge bands). Since the method worked on both scattering and gaseous absorption, two-phase flow application became conceivable such as condensation and evaporation of water vapor, or the spreading of rocket exhaust products, and unburnt fuels.

Ultraviolet absorption measurements with collimated beams proved to be extremely difficult because of the comparatively low levels of the mean radiative power. The commercially available Hannovia lamps and McPherson lamps are much less bright than sources emitting visible light. Also, the small beam diameter (2mm) severely reduces the solid angle that can be used to collect radiation from the source. Therefore, we had unusual low power levels, that is, high shot-noise levels. The usual method of reducing shot noise, using electronic filtering, could be employed only to a limited extent since the bandwidth of the filter must be such that the complete turbulent spectrum is accepted. Thus, the shot noise was one order of magnitude higher than the RMS level of the integrated optical signal. In spite of these limitations, nine out of twelve runs showed the correct convection speed. Later tests used a focused beam system rather than a collimated beam system [13]. This increased the signal to noise ratio by a factor of 200.

IV. CONCEIVABLE IN-FLIGHT EXPERIMENTS

We propose that crossed-beam test arrangements are used in remote sensing missions to monitor horizontal winds, humidity and thermodynamic properties of the earth's atmosphere [14]. Two typical test arrangements are shown in figure 10. One illustrates the local use of ground detectors and the other one a global coverage with orbiting detectors.

Present meteorological sensors are mounted on meteorological towers, balloons, aircraft, and rockets. These monitoring systems have the following inherent limitations:

- (1) Single path experiments,
- (2) Restricted altitude ranges,
- (3) No control over horizontal traverse,
- (4) Interference with the phenomena of interest,
- (5) Large-scale averaging.

Because of these limitations, some meteorological problems partially defy the use of existing instrumentation [15]. Meteorologists have already turned to remote sensing devices to overcome part of these instrumentation problems. It is hoped that remote sensing devices accomplish the following three objectives [16].

- (1) Establish global observation of the entire earth's atmosphere on a regular basis.
- (2) Provide observations for direct use in mathematical prediction models.
- (3) Follow the full life cycle of weather systems such as hurricanes.

In meeting these objectives, one could overcome the two main problems which at present plague numerical weather prediction [16]: (1) insufficient grid points and (2) unknown effect of small scale disturbances on the nonlinear behavior of larger scale motions.

At present a grid of observation stations is available only in North America, Europe, and the northern part of Asia. Except for Australia and very few observation stations in Africa, South America, and Antarctica, the Southern Hemisphere is void of data. Attempts are now being made to measure winds with long-lived constant-pressure balloons, tracked either from the ground or by satellite. The spatial positions of these balloons depend on the circulation pattern and not on the desires of the meteorologist. Any improvement in providing meteorological information at discrete levels in the atmosphere (≈ 50 to 100 mb pressure level), at discrete time intervals (≈ 4 times a day), and with discrete spacing (≈ 200 miles) would be greatly welcomed and would be considered a big leap forward in improving forecasting conditions. The remainder of this paper indicates how crossed-beam test arrangements may be used in remote sensing missions to supply the missing information at the desired location.

The second problem was to estimate the effect of small scale disturbances, such as convective cloud patterns, small vortices, turbulence, etc., on the nonlinear behavior of larger scale motions. Attempts are now being made to estimate such small scale systems from a stationary satellite which takes cloud pictures over the Pacific Ocean. However, commensurate information on winds, temperature, etc., is still lacking. This means that, in addition to the large scale information mentioned previously, small scale measurements should be available for certain time intervals and certain critical regions, which may be specified on short notice by weather prediction centers. Here again, a crossed-beam monitoring system might be the answer. On the following pages we will indicate that scanning crossed-beam systems give turbulence length

scales and wave number components as well as wind information. These results are necessary to study the transfer of kinetic energy between atmospheric motions, which are characterized in terms of macroscales, mesoscales and microscales. Single-point probings such as balloon-borne beam instruments cannot provide this information.

One other important application would be an early warning system for clear-air turbulence. A crossed-beam arrangement with optical detection devices should be able to detect turbulence in atmospheric regions which are "clear" to radar receivers. A space-fixed system might be used to monitor clear-air turbulence above traffic centers, whereas an orbiting system could be used to sweep desired flight paths.

V. EXPECTED OPTICAL SIGNALS

The feasibility and potential of crossed-beam experiments in the lower atmosphere are illustrated in this paper by considering the operation which would be necessary to measure a horizontal wind profile up to altitudes of 30 km. Such crossed-beam arrangements, figure 10, would work whenever detectable space and time variations of emission or extinction processes are common to both beams. This requires local changes in radiative power of sufficient intensity that the change may still be resolved after being transmitted to the distant spectrophotometer. Furthermore, the radiation source should be extended rather than a point source to avoid fluctuations caused by refractive index variations, such as the scintillation of star images. We have therefore tried to answer the following questions:

- (1) What is the mean radiative power of suitable extended radiation sources?
- (2) What modulations of this radiative power can one expect due to atmospheric inhomogeneities which move broadside relative to single beam?
- (3) Are these meteorological modulations above the detector noise levels?

1. Mean Radiance of Extended Natural Sources

Consider a photometer coupled to an astronomical telescope. The detectable radiative power is contributed by all radiative phenomena inside the collimated field of view of the telescope (see figure 11). In atmospheric applications, the detector is placed on either the ground or the orbiting spacecraft as shown in figure 10. Because of light absorption in the atmosphere, remote sensing of meteorological phenomena

inside the atmosphere requires work in regions of the electromagnetic spectrum, where the atmosphere is at least partially transparent. These "optical windows" may be found from typical transmission spectra like the one shown in figure 13. The bottom part of this figure shows the spectral region where suitable windows exist.

Remote sensing within the "optical windows" requires the existence of either man-made or natural radiation sources. The use of man-made sources would severely limit the application of the technique, and point sources such as stars must also be discarded because of scintillation effects. Natural, extended background sources which require no tracking and suffer no scintillation are therefore ideal sources for use in the crossed-beam technique.

The following sources are conceivable:

- (1) Scattered solar radiation
ground detector
- (2) Emission from the atmosphere
- (3) Solar radiation reflected and scattered by the earth's surface
orbital detector
- (4) Thermal radiation from the earth and the atmosphere

All these sources constitute an extended background of radiation. We will discuss the characteristics of these sources that are potentially useful as part of a weather monitoring system. The main results are summarized in table I.

Ground-based detectors (figure 10) can use scattered sunlight and infrared emission from the atmosphere as radiation sources to monitor atmospheric phenomena.

Scattered Sunlight. Solar radiation is both absorbed and scattered in passing through the earth's atmosphere to an extent which varies with the wave length. The earth's surface receives radiation both in the form of a parallel beam of rays from the sun and scattered radiation incident from all points of the sky. The total flux of scattered radiation reaching an object depends on the sun angle, the cloud cover, the terrain reflectance, and the concentration of tracers in the atmosphere. The flux of the scattered radiation is weakly dependent upon earth latitude and more strongly dependent upon sun elevation angle, as shown in figure 12.

Table 1. Estimation of Radiance Available to
Ground and Orbital Detectors

Detector Location	Ground	Ground	Orbit	Orbit
Extended Source	Scattered Sunlight	Ozone Emission	Reflected and Scattered Sun Light	Thermal Emission of Earth
Monochromator Bandpass $\Delta\lambda$	0.38 μ to 0.72 μ	9 μ to 10 μ	0.38 μ to 0.72 μ	8 μ to 12 μ
Estimated Mean Radiance \bar{I}	$4.5 \cdot 10^{-3}$ watts/cm ² ster	$7.8 \cdot 10^{-5}$ watts/cm ² ster	$4.2 \cdot 10^{-3}$ watts/cm ² ster	$4 \cdot 10^{-3}$ watts/cm ² ster
Estimated Modulation in Spectral Radiance i_{RMS}	$4.5 \cdot 10^{-6}$ watts/cm ² ster	$7.8 \cdot 10^{-8}$ watts/cm ² ster	$4.2 \cdot 10^{-6}$ watts/cm ² ster	$4 \cdot 10^{-6}$ watts/cm ² ster
Modulation Bandwidth B	300 cps	300 cps	1000 cps	1000 cps

Influenced by the various parameters mentioned above, scattered solar radiation fluxes have been measured ranging from 0.35 to 2.80×10^{-2} watts/cm² [17]. The same reference reports individual cases where the values of the flux of the scattered radiation exceeds 7×10^{-2} watts/cm². A conservative figure for the flux from a cloudless sky with a solar altitude of 45° would be about 1.4×10^{-2} watts/cm².

In crossed-beam experiments we are not interested in the total flux received from the entire sky (hemisphere = 2π steradian), but only in the sky radiance which is available to the small angle of view $\Delta\alpha$ of a telescope [$4\pi \sin^2(\Delta\alpha/4)$ steradian].

Assuming that Lambert's law gives a reasonable approximation of the angular distribution of scattered sunlight, the radiance measured by a vertically pointing telescope becomes

$$1.4 \cdot 10^{-2} / \pi = 4.5 \cdot 10^{-3} \text{ watts/cm}^2 \text{ steradian.}$$

Of prime importance in our study of the scattered radiation is the radiance available in an emission bandwidth, $\Delta\lambda$. The spectral radiance of scattered radiation is shown in figure 13 for a cloudless sky with the sun at a zenith angle of 45° for an observer located on the earth's surface and at an altitude of 30 km [15]. Taking account of detector response, a useful bandwidth of emission for scattered solar radiation is from 0.38 to 0.72μ with a maximum intensity between 0.4 and 0.5μ . Radiation detected at wave lengths greater than about $2 - 3\mu$ is not due to scattering of solar radiation, but to thermal emission in the atmosphere.

The flux of scattered sunlight is, in first approximation, roughly proportional to the density of the scattering molecules above the detector. At 30 km the atmospheric density is 10^{-2} , that of sea level. Hence, we may expect the local source strength of scattered solar radiation at these altitudes to be of the order of 10^2 times smaller than at sea level. This is found to be so, as reported in [15] and shown in figure 13.

Ozone Emission. Besides scattered sunlight, the ground detector could also detect the thermal emission from the atmosphere. For crossed-beam experiments we need an atmospheric window to "see" through the troposphere. However, there has to be some emission, absorption, or scattering of radiation present for application of the crossed-beam technique. In this study therefore, the feasibility of application of the technique using the 9.6 thermal emission band of ozone as the source of radiation was considered. Since this radiation band falls within the $8\mu - 12\mu$ atmospheric window, measurements throughout the troposphere are possible. This band is clearly indicated by the "dip" in the atmospheric transmission (figure 13). For ground detectors this band is important because:

- (1) It is in a spectral region where it is the only active tracer; there exists no water vapor or strong CO_2 bands to interfere.
- (2) Contributions to the signal at 9.6μ received by a ground detector from altitude ranges 0-10 km, 10-24 km, and above 24 km are at the same order, and thus ozone emission may be used in crossed-beam experiments.

The following table shows the spectral radiance of ozone emission in the 9.6μ band as a function of zenith angle, with the background continuum subtracted [18].

The atmosphere was arbitrarily divided into three layers, and the contribution from each is given.

Table 2

9.6 μ Ozone Emission Intensity (watts cm⁻² ster⁻¹ μ ⁻¹)

Zenith Angle	Ground to Tropopause (0-10 km)	Tropopause to 30 MB (10-24 km)	Above 30 MB (above 24 km)
0	1.6 x 10 ⁻⁵	2.7 x 10 ⁻⁵	3.5 x 10 ⁻⁵
60°	3.0	3.8	4.0
75°32'	5.2	5.2	3.5
80°24'	7.2	5.9	2.8
82°48'	8.7	6.0	2.6

The first line of Table 2 provides an estimate of the total radiance which was measured by a ground detector looking vertically upward through the atmosphere at a wave length of 9.6 microns. If this ozone emission band is taken to be one micron wide, i.e., $\Delta\lambda = 1\mu$, then the total detected intensity will be

$$7.8 \times 10^{-5} \text{ watts cm}^{-2} \text{ ster}^{-1} \mu^{-1}.$$

More recent measurements by Bell et al. (1960) reproduced in the "Handbook of Geophysics and Space Environments" AFCRL, give higher figures for the spectral radiance of the ozone emission. For the zenith direction, the radiance at the middle of the ozone band was measured as 2.5×10^{-4} watts cm⁻² ster⁻¹ μ ⁻¹, and for a zenith angle of 60°, 4.5×10^{-4} watts cm⁻¹ ster⁻² μ ⁻¹ was recorded. However, we have chosen to use the more conservative number above.

Orbital detectors may also detect scattered sunlight and ozone emission. Additional extended radiation sources are provided by reflected sunlight and by the earth's thermal emission. The following discussions are restricted to the same atmospheric windows chosen for discussion of ground detectors, although application of the crossed-beam technique to other wave lengths are in no way ruled out.

Scattered and Reflected Sunlight. The radiation of wavelength λ received by a detector looking toward the earth from an orbiting satellite depends on a large number of factors:

- (1) Intensity of sun's radiation incident at edge of atmosphere at wave length λ .
- (2) Transmission of atmosphere.
- (3) Zenith angle.
- (4) Contribution by scattering from molecules and aerosols.
- (5) Diffuse reflectance of terrain.
- (6) Emission of earth and atmosphere.
- (7) Presence or absence of clouds.
- (8) Spectral bandwidth of detecting system.
- (9) Collector optics.
- (10) Detector sensitivity.

The intensity of the sun's radiation at the edge of the atmosphere and at ground level and diffuse reflectances of different types of earth terrain are given in table 3.

Table 3
Spectral Radiance of Sun at Normal Incidence

<u>Outside Atmosphere</u>	
Wave length (μ)	Intensity watts/cm ² / μ
0.4	1.74 x 10 ⁻¹
0.5	1.96
0.6	1.8
0.7	1.5

<u>At Sea Level-Zenith Angle 60°</u>	
Wave length (μ)	Intensity watts/cm ² / μ
0.4	0.47 x 10 ⁻¹
0.5	1.2
0.6	1.17
0.7	1.11

Table 3 (Continued)

Typical Values of Terrain Reflectance (0.4-0.7 μ)

<u>Terrain</u>	<u>Reflectance</u>
Snow	0.8
Water	0.05
Forests	0.03
Open grassland	0.06
Dark brown soil	0.11

On the basis of these figures, the radiance available to orbital detectors from the sunlit portions of the earth's surface may be estimated. Taking a terrain reflectance of 0.25, the contribution by reflection from the surface will be of the order of

$$\frac{1.8 \times 10^{-1}}{\pi} \times (0.7)^2 \times 0.25 = 7 \times 10^{-3} \text{ watts cm}^{-2} \text{ ster}^{-1} \text{ micron}^{-1}$$

$$= 2.11 \times 10^{-3} \text{ watts cm}^{-2} \text{ ster}^{-1}$$

for the spectral bandpass 0.4 - 0.7 μ . A mean atmospheric transmission of 0.7 is assumed here, corresponding to a zenith angle of the order of 30°.

In addition, there will be a contribution due to scattering by molecules and aerosols in the atmosphere which will be strongly dependent upon the direction of observation, direction of the sun, and also the ground reflectivity. Calculations have been made for a plane parallel Rayleigh atmosphere by Coulson, Dave and Sekera [19] for a large variety of conditions. Assuming a zenith angle of 30°, a ground reflectivity of 0.25 then from tables the radiance seen by a detector looking vertically downward through the atmosphere in the wave length band 0.4 - 0.7 microns will be 4.2×10^{-3} watts cm^{-2} ster^{-1} . This is a lower limit and was used in table 1. The presence of aerosols will increase the scattering contribution and decrease the contribution of reflection of the earth's surface. An upper limit is obtained by assuming a diffuse reflectance of unity, which gives 1.7×10^{-2} watts cm^{-2} ster^{-1} for the same spectral bandwidth.

Thermal Emission from the Earth. Besides reflected and scattered sunlight, the orbital detector could use the thermal emission from the earth as an extended radiation background. Most substances on the earth's surface have nearly unit infrared emissivity. In the relatively transparent infrared regions of the atmosphere and on clear days, this radiation is nearly free to escape unaltered into space. The main variations observed are from equator to pole as the earth's surface temperature changes. The radiance of the sun side of the earth observed outside the earth's atmosphere by a satellite is shown in figure 14. In the transparent regions, the radiance corresponds to a black body at the surface temperature of the earth, while in the strongly absorbing regions, it corresponds to the black-body radiance at stratospheric temperatures. Between 8 and 12 microns, a satellite-borne detector will therefore see the same radiance both on the night and on the day side of the earth. Since the 8 to 12 micron band of emission is near the peak of the black-body radiation, the thermal emission, which is picked up by an orbiting telescope, can be calculated from the black-body curve. The associated radiance is

$$4 \cdot 10^{-3} \text{ watts/cm}^2 \text{ ster.}$$

2. Meteorological Power Modulations

Meteorological modulations of the mean radiative power are produced by the generation, convection and decay of emitting, scattering and absorbing particles which follow the atmospheric motions. The following discussion is restricted to scattering. The only direct measurements of such extinction modulations currently known to us have been made in conjunction with optical communication studies.

Meteorological modulations of a He-Ne laser have been measured over optical paths up to 6.8 km long (mountain range) [20]. The laser output of 0.8 milliwatt was collected by a 24-inch reflecting telescope. By using the full aperture of the telescope, no "spill-over" of the laser light occurred and the attenuation measured by the detector was due to atmospheric attenuation and not to refractive index variations which would cause the bending of the light beam away from the sensor. Figures 15a and 15b give the power spectrum of the intensity fluctuations. The integration, which is outlined in figure 15a, indicates that the ratio of the root-mean-square value to the mean (d.c.) level of the fluctuating signals are on the order of one percent. This one-percent fluctuation is taken as representative of the intensity fluctuations occurring over large atmospheric distances. Over shorter ranges and along paths close to the ground, the fluctuations were of the order of 0.1 percent to 10 percent.

The frequency of these fluctuations should be roughly proportioned to the speed with which atmospheric inhomogeneities are pulled broadside through the laser beam or through the field of view of the detecting system. The range of energy-bearing frequencies for the laser experiments extends from approximately 2 cps to 300 cps for a wind speed of 2 to 4 m/sec (figure 15). For given atmospheric conditions, the upper frequency limit will depend on the beam diameter or on the field of view of the detecting system in a general case. If we take on orbital scanning speed of 8000 m/sec and a field of view equivalent to 50 meters, then frequencies up to 160 cycles per second are to be expected. In the computations of detector noise, a figure of 1000 cps was taken as the upper frequency limit for the orbital case.

Other evidence of fluctuation levels to be expected in atmospheric crossed-beam experiments is available from measured temperature fluctuations. Since in the atmosphere velocities vary much less than the speed of sound, density variations arise from temperature variations. Typically, variations of the order of a few tenths to over one degree centigrade are observed; therefore, these variations correspond to density variations of up to 1 percent. The number density of aerosol particles might be expected to show similar fluctuations.

In fact, as noted above, there is practically no information available on the fluctuations in scattered sunlight recorded by a detector on the ground or in a satellite; it is for this reason that we are now conducting such experiments. The information obtained will serve as input to determine the optimum design for the experiments described in later sections of this paper.

The modulations of radiated power which are produced at higher altitudes are equally difficult to estimate. For scattered sunlight, variations in aerosol concentrations are likely to be the main source of fluctuations at low altitudes. At higher altitudes, fluctuations in air density are more important. This is because above 5 km, the aerosol concentration decreases much more rapidly with altitude than does the air density (figure 16). The contribution to the fluctuating signal, for scattered sunlight, is therefore expected to decrease quite rapidly with altitude; this will limit the maximum altitude for which the cross-correlation technique will permit the signal to be extracted from the noise in reasonable integration times.

This difficulty is not present in the case of ozone emission because of the distribution of ozone in the atmosphere. The altitude of maximum ozone concentration varies from about 10 to 30 kilometers depending on latitude, time of year, etc. Thus, ozone is likely to be useful in tracing atmospheric motions at higher altitudes. For the calculations in this paper, fluctuations in ozone concentration are assumed to be similar to those in air density, that is, of the order of 1 percent.

In our estimate of the expected modulation amplitude i_{RMS} , we tried to account for the decrease of tracer concentration with altitude by choosing $i_{\text{RMS}}/\bar{I} = 10^{-3}$ as a reference value. The associated meteorological modulations of the mean radiative power are summarized in table 1.

3. Detector Noise

Although the nature of the cross-correlation technique permits signals that are buried in the noise to be measured, it is very desirable that the above meteorological modulations of the incident radiative power produce output signal fluctuations, i_{RMS} , larger than the detector noise, i_d . In this case, the feasibility of the crossed-beam technique, as applied to the study of atmospheric problems, will be determined by the magnitude of the background fluctuations and the turbulence length scales along each of the crossed beams. The space-time variations of scattered sunlight and thermal radiation represent an output from integrated light sources and should not vary as much as the local emission and extinction processes of interest. The number of correlation volumes along the optical path should be small enough to avoid cancellation due to integrating over too many statistically independent parts. Since turbulence is mostly restricted to a few layers, cancellation should be no problem. Even if cancellation occurs, it can be partially eliminated by acting on the optical path length. Therefore, the main limiting factor appears to be the detector noise.

The detector noise has been calculated for detectors operating in the visible ($\lambda = 0.55\mu$) and infrared ($\lambda = 9.6\mu$); the results are summarized in table 4.

The sizes of the collecting mirrors are chosen with regard to the final signal/noise ratios and are no larger than the mirror systems in the OAO series of orbiting astronomical observatories. The choice of field of view of the optical systems is based on assumed average integral length scale of 300 meters. This latter figure agrees very well with the scales of clear-air turbulence measured by Burns and Rider [21]. To resolve 300-meter scales, a field of view corresponding to approximately 50 meters is desirable; this figure at the tropopause gives the field of view figures given in the table.

The values of mean radiance used in the table and discussed in previous sections of this paper, together with the field of view and the size of the collecting mirror, permit the radiation received by the detector to be calculated.

In the visible region of the spectrum, phototubes or photomultipliers are the appropriate detectors to use, and for the light levels in question, the main source of noise in the output signal will result from the randomness of the emission of electrons from the photo-

Table 4
Detector Operation and Noise

Operation	Visible Light ($\lambda = 0.55\mu$)		Infrared ($\lambda = 9.6\mu$)	
	Ground	500km Orbit	Ground	500km Orbit
Mirror Cross-section [cm ²]	10 ²	10 ⁴	10 ⁴	10 ⁴
Field of View Minutes of arc ($\Delta\alpha$) $4\pi \sin^2(\Delta\alpha/4)$ ster.	15' $1.5 \cdot 10^{-5}$	0.34' $7.8 \cdot 10^{-9}$	15' $1.3 \cdot 10^{-5}$	0.34' $7.8 \cdot 10^{-9}$
Mean Radiance [watts/cm ² ster]	$4.5 \cdot 10^{-3}$	$4.2 \cdot 10^{-3}$	$7.8 \cdot 10^{-5}$	$4 \cdot 10^{-3}$
Minimum of Mean Radiative Power \bar{I} [watts]	$5.8 \cdot 10^{-6}$	$3.3 \cdot 10^{-7}$	10 ⁻⁵	$3.1 \cdot 10^{-7}$
Photon Current $\frac{\bar{I}}{h\nu}$ [Photons/sec]	$16 \cdot 10^{12}$	$8.9 \cdot 10^{11}$	$4.8 \cdot 10^{14}$	$1.5 \cdot 10^{13}$
Modulation Bandwidth B [cps]	300	1000	300	1000
Detector Mean Signal \bar{I}_d	Output $2.6 \cdot 10^{-7}$ Ampere	Output $1.4 \cdot 10^{-8}$ Ampere	Input 10 ⁻⁵ Watt	Input $3.1 \cdot 10^{-7}$ Watt
Detector Noise i_d	Output $5 \cdot 10^{-12}$ Ampere	Output $2.1 \cdot 10^{-12}$ Ampere	Noise equivalent power $1.7 \cdot 10^{-10}$ Watt	Noise equivalent power $3.2 \cdot 10^{-10}$ Watt
Atmospheric Modulation i_{RMS}	Output $2.6 \cdot 10^{-10}$ Ampere	Output $1.4 \cdot 10^{-11}$ Ampere	Input 10 ⁻⁸ Watt	Input $3.1 \cdot 10^{-10}$ Watt
Signal/Noise i_{RMS}/i_d	52	6	59	1

cathode, or "shot-noise." The number of photons incident on the photocathode may be simply calculated by dividing the energy per photon into the incident radiant flux. At 0.55μ the energy per photon is given by

$$h\nu = 3.9 \times 10^{-19} \text{ watt-seconds.}$$

If photocathodes of the tri-alkali type are used, the average quantum efficiency Q over the visible spectral region will be of the order of 10 percent. That is, for each ten incident photons, one photoelectron will, on the average, be emitted. The cathode current is therefore given by

$$\bar{I}_d = Q N_e e, \quad (29)$$

where Q is the quantum efficiency, N_e is the number of photons incident per second, and e is the electronic charge. The mean square noise associated with this cathode current is

$$\bar{i}_d^2 = 2e \bar{I}_d B = 32 \times 10^{-20} \bar{I}_d B, \quad (30)$$

where B (cps) is the electronic bandwidth of the detecting system.

For infrared detectors, the noise is listed in terms of the equivalent radiative input power i_d , which would produce the same RMS value of the detector output in an imaginary experiment, conducted with a "perfect" noise-free detector. The best detector to use in the wavelength range $8 - 12\mu$ is a mercury-doped germanium-type of photoconductive detector [22], which for a detector 0.1 cm^2 will have a noise equivalent input equal to

$$i_d (\text{watt}) = 1 \times 10^{-11} \sqrt{B \text{ cps}}. \quad (31)$$

The bottom line of table 4 gives the resulting signal-to-noise ratio (i_{RMS}/i_d) for the four systems, where the modulation in the incident intensity at the detector due to the atmosphere is assumed to be 0.1 percent in each case. It appears that the feasibility of the application of the crossed-beam technique to the atmosphere will not be limited by detector noise unless the signal fluctuations caused by atmospheric effects are much smaller than presupposed here.

VI. THEORY OF CROSSED-BEAM SCANNING

In the global coverage of vast and sparsely instrumented areas, environmental monitoring systems would have to gather information quickly enough that the results can be used for the prediction of weather and the prediction of navigational and communication hazards

such as clear-air turbulence. This consideration leads to the extension of the crossed-beam concept from space-fixed beams to scanning or sweeping beams. M. Wolf [2] has already successfully operated a scanning crossed-beam system. He rotated two ground detectors in such a way that the beam intersection point moved along a horizontal path at approximately 100 km altitude. A cross correlation of the optical fluctuations from the night-glow emission gave the height of the air-glow phenomenon with great accuracy. We now extend the idea of crossed-beam scanning to include systematic beam separations in space and time and the measurement of turbulence parameters. We will indicate how the two-beam product mean values from moving beams are to be interpreted in terms of convection speeds, turbulence length scales, and space correlations (wave number components). The theoretical treatment is kept general and could be applied to orbital as well as ground detectors.

1. Geometry of Scanning Beams

We define the scanning or sweeping motion of crossed beams by the motion of the points of minimum beam separation A and B. The straight line which goes through these two points had been introduced as the beam normal. In case of crossed-beam scanning, this normal moves broadside and sweeps out a certain surface. We have chosen to classify crossed-beam systems in terms of the motion of the beam normal and through the orientation of the beams relative to the surface of the sweeping normal. This gives a unified treatment which can be applied to both orbital and ground detectors. The following discussions are restricted to a crossed-beam system where both the speed of the normal and the orientation of the beams relative to the surface of the normal are time invariant. Such crossed-beam systems, shown in figure 17, may be compared to the translation of a rigid mechanical structure. The beam arrangement is thus uniquely classified in terms of the following invariant parameters:

- (a) The scanning speed U_B describing the speed of the point B of minimum beam separation inside the surface of the sweeping normal.
- (b) The inclination β of the path of B relative to the beam front, that is, relative to a plane which is parallel to both beams. The path of point B will be called the "intersection path."
- (c) The inclinations α_A and α_B of the two beams relative to the surface of the sweeping normal.

The motion of the individual beam is now described in two different space-fixed coordinate systems, also shown in figure 17. The first system is needed to describe the position of a beam point relative to the earth's surface. The z-axis points vertically upward and the x-axis follows the line of minimum beam separation. The y-axis follows from the condition that the x,y,z system should be an orthogonal system. The coordinates ξ, η, ζ of the second system are defined in terms of the position which the sweeping beams occupied at the instant $t = 0$, that is, at the start of the experiment. The ξ -axis follows the beam normal, the η -axis the leading beam, and the ζ -axis the trailing beam. This system is not necessarily orthogonal, since the angle

$$\alpha_{AB} = \pi - \alpha_A - \alpha_B \quad (32)$$

between the beams is not necessarily a right angle. The relation between the two coordinate systems follows from geometrical considerations and may be given as follows:

$$\begin{aligned} \vec{x}(\xi) &= x_0 + \xi \\ y(\xi) &= y_0 + \eta \cos \alpha_B - \zeta \cos \alpha_A \\ z(\xi) &= z_0 + \eta \sin \alpha_B + \zeta \sin \alpha_A. \end{aligned} \quad (33)$$

Here \vec{x}_0 denotes the origin of the ξ, η, ζ system, that is, the position of the moving point B at time zero. The trajectory of point B follows the "intersection path." Each point on this path shall be denoted by the path length p relative to the point \vec{x}_0 .

$$\vec{x}_B(p) = \begin{bmatrix} x_0 \\ y_0 \\ z_0 \end{bmatrix} + p \begin{bmatrix} \sin \beta \\ \cos \beta \\ 0 \end{bmatrix}. \quad (34)$$

The scanning speed U_B describes a velocity vector which follows the intersection path. This vector may thus be denoted by

$$\vec{U}_s = \begin{bmatrix} U_s \\ V_s \\ W_s \end{bmatrix} = U_B \begin{bmatrix} \sin \beta \\ \cos \beta \\ 0 \end{bmatrix}. \quad (35)$$

Similar trajectories can be written for any other point of the trailing beam "1". At time zero this beam coincides with the ζ -axis and may thus be found at position $\vec{x}(0,0,\zeta)$. The trajectory of this point is then given by

$$\vec{x}_1(\zeta, p) = \vec{x}(0,0,\zeta) + \vec{x}_B[p(t)] = \begin{bmatrix} x_1(\zeta, t) \\ y_1(\zeta, t) \\ z_1(\zeta, t) \end{bmatrix} = \begin{bmatrix} x_0 + p \sin \beta \\ y_0 - \zeta \cos \alpha_A + p \cos \beta \\ z_0 + \zeta \sin \alpha_A \end{bmatrix}. \quad (36)$$

The fluctuations $i_1(t)$, which are recorded for the trailing beam, follow from the optical integration along this beam.*

$$i_1(t) = \langle I_1 \rangle \int_{-\infty}^{\infty} k(\vec{x}_1(\zeta, t); t) d\zeta. \quad (37)$$

Similarly, an arbitrary point on the leading beam "2" is denoted by the beam length η and moves along the trajectory.

$$\vec{x}_2(\xi, \eta, t) = \vec{x}(\xi, \eta, 0) + \vec{x}_B[p(t)] = \begin{bmatrix} x_2(\xi, \eta, p) \\ y_2(\xi, \eta, p) \\ z_2(\xi, \eta, p) \end{bmatrix} = \begin{bmatrix} x_0 + \xi + p \sin \beta \\ y_0 + \eta \cos \alpha_B - \xi \cos \alpha_A + p \cos \beta \\ z_0 + \eta \sin \alpha_B + \xi \sin \alpha_A \end{bmatrix}. \quad (38)$$

The optical integration along the leading beam can thus be expressed by

$$i_2(t) = \langle I_2 \rangle \int_{-\infty}^{\infty} k(\vec{x}_2(\xi, \eta, p); t) d\eta. \quad (39)$$

* Light source fluctuations are neglected since they are mostly uncorrelated; i.e., a further noise contribution, which is suppressed by correlation techniques. The operator $\langle \rangle$ is used for the time average of moving beams.

The two-beam product mean value of a sweeping crossed-beam system follows from the time average of the instantaneous product

$$\begin{aligned}
 R(\xi, \tau = 0) &= \langle i_1(t) i_2(t) \rangle_{\xi} = \int_{-\infty}^{\infty} \int_{-\infty}^{\infty} \langle k[\vec{x}_1(\zeta, p(t)); t] k[\vec{x}_2(\xi, \eta, p(t)); t] \rangle d\zeta d\eta \\
 &= \int_{-\infty}^{\infty} \int_{-\infty}^{\infty} R_m(\vec{\xi}) d\eta d\zeta.
 \end{aligned} \tag{40}$$

One finds that the two-beam product mean value is an area integral over a great number of observer pairs each of which travels parallel to the intersection path.

2. Length Averages of Frozen Patterns

The individual observer averages over the fluctuations which he encountered along his trajectory. The fluctuations are produced by scanning inhomogeneous spatial distribution of radiative power and by true temporal variations as communicated by a space-fixed observer. We have thus a mixed space and time average. This averaging process is analogous to the way the human eye evaluates a TV picture. Each frame of the television is displayed on the screen by a rapidly moving electron beam. To the viewer the modulations of the electron beam are displayed so rapidly that the resulting image appears as a "frozen pattern"; that is, like a flashlight image. Although the information which is displayed by the scanning beam was recorded as a time function, its interpretation assumes a space history. Only by comparing several frames is it possible to detect generation, convection, and decay of new patterns.

We now assume that an observer pair scans so rapidly that the associated two-point product mean value R_k closely approximates a length average \bar{R}_k^p along the observer trajectory. This means replacing the time history of a moving beam point with the flashlight image ($t = 0$) at all points P along its trajectory.

$$\begin{aligned}
 R_m(\vec{\xi}) &= \langle k[\vec{x}_1(\zeta, p(t)); t] k[\vec{x}_2(\xi, \eta, p(t)); t] \rangle \\
 &\approx \lim_{P \rightarrow \infty} \frac{1}{P} \int_{p=0}^{p=P} k(\vec{x}_1(\zeta, p); t = 0) k(\vec{x}_2(\xi, \eta, p); t = 0) dp.
 \end{aligned} \tag{41}$$

For convenience, this length average will be denoted by the operator "-p", i.e., $R_m \simeq \bar{R}_k^p$. The last approximation is valid whenever the spatial

distribution or "pattern" of k is frozen [$k(\vec{x}, t) = k(\vec{x}, 0)$] over the time period of the scan. It is also valid if a frozen pattern is convected at a constant speed U_C , since this would alter only the effective scanning speed of the moving observer pair. The last equation is therefore valid for all convected frozen patterns; that is, for all possible directions of the convection speed. Furthermore, it can be shown that the pattern does not have to be entirely frozen. The approximation of length averages is still good as long as the temporal variations which are experienced by a third observer travelling with the convection speed can be treated as small perturbations and are statistically stationary.

Replacing the time average of scanning observers with a length average over the observer's trajectory leads to the following expression for the two-beam product mean value of a rapidly scanning system:

$$\langle i_1(t) i_2(t) \rangle_{\xi} = \langle I_1 \rangle \langle I_2 \rangle \int_{-\infty}^{\infty} \int_{-\infty}^{\infty} \bar{R}_k^P(\vec{\xi}) d\eta d\xi = \quad (42)$$

$$\langle I_1 \rangle \langle I_2 \rangle \int_{-\infty}^{\infty} \int_{-\infty}^{\infty} \overline{k(\vec{x}_1(\zeta, p), t = 0) k(\vec{x}_2(\xi, \eta, p); t = 0)}^P d\eta d\xi.$$

In the above averaging procedure, it was always assumed that no time lag was introduced in the data reduction. However, in space-fixed crossed-beam arrangement, the systematic variation of time lags was required to separate convection and generation and decay processes and to measure the convection speed. Similar interpretations of temporal correlation, which hold for moving beams, will now be discussed.

The fluctuations of radiative power which produce the signal $i_2(t)$ along the leading beam have been on another position $\vec{x}_{2, \text{imag}}$ at the time $t - \tau$. In case of a convected frozen pattern, this earlier position is parallel to the leading beam and may be found by tracing back the scanning motion \vec{U}_s and the convective motion $\vec{U}_C \equiv (U_C, V_C, W_C)$. The signal of the delayed beam $i_2(t - \tau)$ is thus identical with the signal from an imaginary undelayed beam, each point of which could be found by the translation

$$\vec{x}_{2, \text{imag}}(\xi, \eta; p, \tau) = \vec{x}_2(\xi, \eta; t(p)) - (\vec{U}_s + \vec{U}_C) \tau. \quad (43)$$

It follows that the above optical integration of two-beam product mean values, equation (42) can be extended to the analysis of a delayed beam, if one replaces \vec{x}_2 with $\vec{x}_{2, \text{imag}}$.

$$\langle I_1 \rangle \langle I_2 \rangle \int_{-\infty}^{\infty} \overline{k(\vec{x}_1(\xi; p); 0) k(\vec{x}_{2, \text{imag}}(\xi; \eta, p; \tau); 0)}^p d\eta d\xi. \quad (44)$$

The interpretation of this two-beam product mean value follows in analogy to the discussion of space-fixed beam by considering the two-point product mean value between the two points A_i and B_i , which are defined through the minimum separation $\xi(\tau)$ between the trailing beam and the imaginary beam. The position of these two points is indicated on figure 18 by the projections of the imaginary beam into the side view and top view of the plane of the sweeping normal. The figure shows that the two pairs of points A_i , B_i and A , B differ by a translation and a change of separation distance. The translation occurs inside the beam front and may be characterized by its Z and Y components.

$$\Delta z(-\tau) = z_{B_i} - z_B = \frac{(V_s + V_C) \tau}{\cot \alpha_A + \cot \alpha_B} \quad (45)$$

$$\Delta y(-\tau) = y_{B_i} - y_B = \frac{(V_s + V_C) \cot \alpha_B}{\cot \alpha_A + \cot \alpha_B} \tau. \quad (46)$$

The change in separation distance is given by

$$\Delta \xi(-\tau) = \xi_{A_i} - \xi_A = -\frac{U_s + U_C}{V_s + V_C} \Delta y = \frac{\cot \alpha_B}{\cot \alpha_A + \cot \alpha_B} (U_s + U_C)(-\tau). \quad (47)$$

As long as the frozen pattern of k is statistically homogeneous over the beam front, a translation by $-\Delta z$, $-\Delta y$ would not affect the two-point product mean value. However, this translation brings the pair $A_i B_i$ back to the original normal (i.e., $\eta = \xi = 0$). In fact, the translated point B_i coincides with B . The translated point A_i , which is denoted in figure 18 by C , defines the new beam separation

$$\xi^*(-\tau) = \xi + \Delta \xi(-\tau) = \xi + C_{AB} (U_B \sin \beta + U_C)(-\tau), \quad (48)$$

where the constant C_{AB} abbreviates the cotangent factor

$$C_{AB} = \frac{\cot \alpha_B}{\cot \alpha_A + \cot \alpha_B}. \quad (49)$$

The only effect of a time delay is thus to change the actual beam separation, ξ , to the effective, $\xi^*(\tau)$. The approximation of two-point product mean values may therefore be extended from space-fixed to moving beams in the following way:

$$\frac{\langle i_1(t) i_2(t + \tau) \rangle_{\xi}}{\langle i_1(t) i_2(t) \rangle_{\xi}} \approx \frac{\bar{R}_k^P(\xi^*(\tau); \eta = 0; \zeta = 0)}{\bar{R}_k^P(\xi; \eta = 0, \zeta = 0)} = \quad (50)$$

$$\frac{k(x_0 + p \sin \beta, y_0 + p \cos \beta; z_0; 0) k(x_0 + p \sin \beta + \xi^*(\tau); y_0 + p \cos \beta, z_0; 0)^P}{k(x_0 + p \sin \beta, y_0 + p \cos \beta; z_0, 0) k(x_0 + p \sin \beta + \xi; x_0 + p \cos \beta; z_0; 0)^P}$$

In a physical sense the time lag τ_M is needed for the combined motions $U_S + U_C$ to cover the original beam separation, ξ . The delayed leading beam then intersects the undelayed trailing beam and the correlation becomes a maximum, since the two points of minimum separation sweeps the same eddies. The convection speed is thus measured by averaging over a row of eddies along the intersection path whereas space-fixed beams average over a single row of moving eddies, which pass a fixed observation point at different times.

3. Interpretation of Two-Beam Product Mean Values

The above approximation of space correlation curves, equation (50), allows several important applications. The first application is the measurement of convection speeds. It follows from the fact that space correlation curves have a maximum at zero space lag. Therefore, the time lag $T_M(\xi)$, which is indicated by the maximum of the temporal beam correlation curve $\langle i_1(t) i_2(t + \tau) \rangle_{\xi}$, should correspond to $\xi^* = 0$.

$$\xi^*(\tau_M) = 0 = \xi + C_{AB} (U_C + U_B \sin \beta) \tau_M. \quad (51)$$

This is an equation which may be solved for the group velocity component:

$$U_C = \frac{\xi}{C_{AB} \tau_M(\xi)} - U_B \sin \beta. \quad (52)$$

The associated estimates of group velocities are graphically illustrated in figure 19. In equation (52), the second term, $U_B \sin \beta$, corrects for the beam motion. If this term is large compared to the group velocity,

$$|U_B \sin \beta / U_C| = |U_s / U_C| \geq 5, \quad (53)$$

then the measurement of U_C becomes difficult since it involves the subtraction of two large quantities of about equal magnitude. The scanning speed U_B must be much larger than the convection speed U_C to justify the assumption of a frozen pattern. Therefore, the last inequality implies that β must always be a small angle. In other words, the beam front has to move almost parallel to itself.

The second application is the estimate of the integral length scale L_x . Since the two-beam product mean value is proportional to the space correlations curve $\bar{R}_k^P(\xi^*)$, the normalized space correlation curve can be approximated by normalizing the two-beam product mean values with their maximum

$$\rho(\xi^*) = \frac{\tau - \tau_M(\xi)}{U_C} = \frac{\bar{R}_k^P(\xi^*, 0, 0)}{\bar{R}_k^P(0, 0, 0)} \approx \frac{\langle i_1(t) i_2(t + \tau) \rangle_\xi}{\langle i_1(t) i_2(t + \tau_M(\xi)) \rangle_\xi}, \quad (54)$$

and by plotting this coefficient as a function of the effective space lag ξ^* . Once the convection speed U_C is known, this lag may be calculated without using the scanning speed, U_B . Substituting equation (51) into equation (48) shows

$$\xi^* = \frac{\tau - \tau_M(\xi)}{U_C}. \quad (55)$$

The plot of space correlation functions is illustrated in figure 20. The integral length scale, L_x , in the direction of the beam normal follows from integration

$$L_x = \frac{1}{2} \int_{-\infty}^{\infty} \phi(\xi^*) d\xi^*. \quad (56)$$

The third application is the estimate of three-dimensional wave number components. The components result, if one wants to describe the space history of a frozen pattern of extinction coefficients $k(\vec{x}, t = 0)$ through a superposition of harmonic waves. Each of these waves is characterized by the number of cycles per unit length ψ_1, ψ_2, ψ_3 which may be oriented in either the $\xi, \eta, \text{ or } \zeta$ direction. The individual wave number component, S_k , denotes the mean square amplitude of such an individual wave and follows from a three-dimensional Fourier transform of the two point product mean value.

$$S_k(\vec{\psi}) = \frac{1}{8\pi^3} \int_{-\infty}^{\infty} \int_{-\infty}^{\infty} \int_{-\infty}^{\infty} \bar{R}_k^P(\xi^*(\tau); \eta, \zeta) e^{-i\vec{\xi} \cdot \vec{\psi}} d\zeta d\eta d\xi. \quad (57)$$

For wave fronts which are parallel to the plane of the beams, we get $\psi_2 = \psi_3 = 0$, and the inner two integrals describe nothing but an integration over the beam front which is automatically performed.

$$\begin{aligned} \int \int \bar{R}_k^P(\xi^*) e^{-i\vec{\xi} \cdot \vec{\psi}} d\eta d\zeta &= e^{-i\xi^* \psi_1} \int_{-\infty}^{\infty} \int_{-\infty}^{\infty} \bar{R}_k^P(\vec{\xi}^*) d\eta d\zeta \\ &= \frac{\langle i_1(t) i_2(t + \tau) \rangle_{\xi}}{\langle I_1 \rangle \langle I_2 \rangle} e^{-i\xi^* \psi_1}. \end{aligned} \quad (58)$$

Substituting into the previous equation gives the three-dimensional wave number component by a one-dimensional integration

$$S_k(\psi_1, 0, 0) = \frac{1}{8\pi^3} \int_{-\infty}^{\infty} \frac{\langle i_1(t) i_2(t + \tau(\xi^*)) \rangle_{\xi} e^{-i\psi_1 \xi^*}}{\langle I_1 \rangle \langle I_2 \rangle} d\xi^*. \quad (59)$$

All properties of the integrand are experimentally accessible to a moving crossed-beam system.

The fourth application is an estimate of the normalized power spectrum. Consider several crossed-beam systems with different beam separations, $\xi = \xi_0, \xi_1, \xi_2, \dots$, which scan the same integration path simultaneously. According to equation (54), the associated temporal correlation curves $R_S(\tau)_{\xi_i} = \langle i_1(t) i_2(t + \tau) \rangle_{\xi_i}$ should all collapse into a single curve if they are translated along the time-lag axis until the maximum coincides with the ordinate. In other words, each of the individual space-time correlations $R_S(\tau)_{\xi_i}$ could be generated by translating the autocorrelation $R_S(\tau)_{\xi=0}$ by the amount $\tau_M(\xi)$. This is indicated in figure 19 by the dashed curves and follows from the assumptions of a frozen pattern. Therefore, by replotting the normalized two-beam product mean value of a single run $\xi = \xi_i$ as a function of the "retarded time lag,"

$$\tau^* = \tau - \tau_M(\xi_i) \quad (60)$$

should give a curve $\varnothing(\tau^*)$ which closely resembles the normalized autocorrelation function. The Fourier transformation of this curve should then give an estimate of the normalized power spectrum

$$S_k(f) = \frac{1}{2\pi} \int_{-\infty}^{\infty} \varnothing(\tau^*) e^{-i2\pi f \tau^*} d\tau^*. \quad (61)$$

The consideration of several simultaneously estimated time correlations curves $R_S(\tau)_{\xi_i}$ also implies a lower limit on the scanning speed. The assumption of a frozen pattern is obviously wrong if the individual curves $R_S(\tau)_{\xi_i}$ depart considerably from the translated autocorrelation $R_S(\tau)_{\xi=0}$. This case is illustrated in figure 19 for $\xi = \xi_2$. The concept of a frozen pattern therefore seems justified only as long as the range of time lags used is small compared to the eddy lifetime. In the atmosphere, eddy lifetimes are usually in excess of 5 minutes, except for layers very close to the ground. On the other hand, our wind tunnel tests suggest that one would probably have to scan over 50 statistically independent regions to retrieve the local information. An average integral length scale of $L_y = 300\text{m}$ [21] gives a region of $L = 50L_y = 15\text{ km}$ length. To scan this region in a tenth of the average lifetime, one needs a scanning speed in excess of $15\text{ km}/0.5\text{ min} = 0.5\text{ km/sec}$.

4. Measurement of Altitude Profiles

It remains to consider the altitude variation that is introduced when setting a time lag. The convection speed is determined from a single time lag τ_M , and its value belongs to the altitude that is indicated by τ_M ,

$$h(\tau_M) = h(\tau = 0) + \frac{V_s + V_C}{\cot \alpha_A + \cot \alpha_B} \tau_M. \quad (45)$$

If one wants to measure an altitude profile of convection speeds in a single sweep, one needs several independent detectors which view the altitude range simultaneously. Each of these detectors should indicate a correlation maximum at a different τ_M . One easy solution is suggested by equation (51). All it takes is to set the photodetectors at different inclinations β against the flight path. Since all of these inclinations are small, as discussed previously, this can be accomplished using only one telescope. One simply collects the radiative power from several off-axis pin-holes in the focal plane of the collecting mirror, as shown in figure 21.

Multiple recorders are mandatory when measuring the space correlation $R_S(\tau^*)$. The calculation of integral length scales, equation (51), and wave number components, equation (59), requires a knowledge of the spatial beam correlation $R_S(\xi^*)$ over the entire range of space lags,

$$\xi_{\max}^* \leq \xi^* \leq \xi_{\min}^*, \quad (62)$$

where $\phi(\xi^*)$ is not zero. The associated range of time lags is fixed by the convection speed and cannot be shortened by special test arrangements.

$$\frac{\tau_{\max} - \tau_{\min}}{\xi_{\max}^* - \xi_{\min}^*} = \frac{1}{U_C}. \quad (63)$$

Typical time lag intervals may be derived setting $\xi_{\max} - \xi_{\min} < 3L_x \leq 1000M$ and $U_C \leq 100M/sec$. They are of the order of 10 seconds, which is much too long when considering the altitudes that are covered meanwhile by scanning speeds in excess of 0.5 km/sec (orbital speed 8 km/sec). Instead, one has to break up the required time lag interval into subintervals of

length $\Delta\tau$, which are derived from the permissible altitude error Δh as given by equation (45).

$$\Delta\tau = \frac{\cot \alpha_A + \cot \alpha_B}{V_s + V_C} \Delta h. \quad (64)$$

One independent photodetector $\ell = 1, 2, 3, \dots$, is required to cover the lag interval $(\ell - 1) \Delta\tau \leq \tau \leq \ell \Delta\tau$. The inclination β_ℓ of the individual detector has to be chosen such that a maximum of the time correlation $R_S(\tau)$ is falling into the interval. This leads to the condition

$$\tau_M(\beta_\ell) \approx (\ell - \frac{1}{2}) \Delta\tau \quad (65)$$

which is sufficient to calculate β_ℓ . Substituting equation (65) into equation (51), solving for β_ℓ and using the expressions for C_{AB} , equation (49), and $\Delta\tau$, equation (64), gives the expression

$$\sin \beta_\ell = - \frac{1}{U_B} \left\{ U_C + (V_s + V_C) \operatorname{tg} \alpha_B \frac{\xi}{(\ell - \frac{1}{2}) \Delta h} \right\}. \quad (66)$$

Choosing the inclinations of the individual photodetectors according to equation (66) guarantees that a maximum $\tau_M(\beta_\ell)$ will be found (that is, a group velocity measurement) in atmospheric layers of thickness Δh . Furthermore, the associated retarded space lags $\xi_\ell^* = \xi(\tau_M(\beta_\ell))$ are spread throughout the desired range of retarded space lags. This procedure also reduces the requirement of homogeneity inside the wave front. Homogeneous behavior is demanded only on the now small translations $\Delta z(\Delta\tau)$ and $\Delta y(\Delta\tau)$.

VII. STEP-BY-STEP SIMULATION OF IN-FLIGHT EXPERIMENTS

Having developed the interpretation of scanning beams, it remains to indicate how the underlying motion of a rigid beam structure can be activated in practice. The measurement of convection speeds, turbulence length scales, and wave number components requires a beam normal which moves broadside through the atmosphere at a scanning speed in excess of 0.5 km/sec. Furthermore, the telescope which defines this normal was restricted to a translation. However, a rotation of the beam structure

around the normal will not change the optical integration over the beam front. Therefore, the telescope motion may be characterized by the conditions α_{AB} , and β must be invariant. Such motion can be achieved with both orbiting and ground detectors. The associated test arrangements are illustrated in figure 22. Using such arrangements has the great advantage that orbital experiments can be simulated and checked out in ground experiments.

1. Test Arrangements

For orbiting telescopes, the beam separation distance, ξ , can be kept constant if the two detectors orbit at the same speed, that is, at the same height. The path of the normal is then horizontal and the surface of reference coincides with surfaces of constant altitude. For ground detectors, a very similar sweep can be arranged by separating the two telescopes by a baseline b and by rotating both beams at the same rate ($\dot{\alpha}_A = \dot{\alpha}_B = \dot{\alpha} = \text{const}$). In this case, the normal is also horizontal and sweeps along a circular arc such that the surface of reference almost coincides with a horizontal plane. The main difference between orbiting and ground detectors is not in the individual sweep but in the way in which the length averages of the two-beam product mean value are established. Orbiting detectors allow averaging over a single horizontal path of infinite length. Ground detectors average over a finite portion of a circular arc, the length of which is determined primarily by the telescope baseline b . However, infinite statistical information can still be collected if one sweeps repeatedly and includes these repeated runs in the averaging procedure. Both averaging procedures give identical results if the pattern of turbulence is spatially homogeneous over the interval of the orbital sweep or if it can be made homogeneous by subtracting large scale, inhomogeneous "means."

2. Preliminary Specifications

We have tried to specify the crossed-beam test arrangements, shown in figure 22, in terms of the independent variables which describe the telescope operation and/or adjustment. These variables are as follows:

λ	optical wavelength set by monochromator
b	baseline or distance between telescopes
α_{AB}	beam intersection angle
U_B	scanning speed that is the speed of the moving normal
ξ	beam separation along beam normal defined by points of minimum beam separation

- τ electronically introduced time lag between beams
- β inclination between the plane of the beams and the path, which is followed by the point of minimum separation
- N number of desired altitude positions, defining number of photodetectors in local plane of telescope
- P interval of intersection path used in averaging procedures

Table 5

Independent Variable	Minimum or Lower Limit	Maximum or Upper Limit	Tolerance Given by	Comment
Optical Wave length λ	0.38 μ	0.72 μ	Entire window for particulate tracers	Visible window
	8 μ	12 μ	For gaseous tracers	Infrared window
Telescope Separation b	$2 \cot \alpha h_{\min}$	$2 \cot \alpha h_{\max}$	Position error $\Delta l = \Delta x$	h is the distance between the beam intersection path and the baseline.
Beam Intersection Angle α_{AB}	15°	75°	Altitude error $\Delta \alpha = 2 \cos^2 \alpha \frac{\Delta h}{b}$	Depends on pointing accuracy
Beam Separation ξ_0	$-2 L_x$	$2 L_x$	$\Delta \xi_0 \leq L_x/5$ (beam diameter)	L_x is the length scale. The beam diameter factor 1/5 is obtained from wind tunnel experiments.
Time lag $ J $	0	$\frac{\xi_{\max} - \xi_{\min}}{U_C} \approx 2 L_x / U_C$	$\Delta \tau = L_x / 5 U_B$	L_x and U_B depend on applications.
Inclination of intersection path with beam plane $ \beta $	$2 \left \frac{U_C}{U_B} \right $	$10 \left \frac{U_C}{U_B} \right $	$\Delta \beta = 2 \Delta \xi_0 / b$ $= \frac{2}{5} L_x$	Equation for $C_{AB} = 1/2$ sets angle of view or horizontal pointing accuracy.
Number of photodetectors	5	depends on hardware and receiver	-	At least five points on a curve to find a maximum
Length of intersection path p	Not known length scale of homogeneous trend $> L_x$	Not known - depends on correlation maximum and receiver noise	$\Delta L = L_x$	One sweep from orbit or pieces of repeated sweeps from ground
Scanning speed	0.5 km/sec	8 km/sec (Orbital speed)	$\frac{1}{5} U_B$	Tolerance depends on application

The desired test arrangement can now be specified in terms of the lower limit (minimum), upper limit (maximum), and tolerance (Δ) which are required for each of the independent variables. These limits and tolerances depend on the desired applications. The considerations of the previous sections allow us to establish rough estimates, the expressions of which are listed in table 5.

The minimum spacing of space lags, $\Delta\xi_0$, has been determined in our wind tunnel tests, which seem to indicate that $\Delta\xi_0 = 1/5 L_x$ gives satisfactory space correlation curves. The tolerance on time lag, $\Delta\tau$, is identical with the sampling period of the A/D converter. It has been approximated by the time the beams would need to scan over a space lag interval.

$$\Delta\tau = \Delta\xi_0/U_B \approx \frac{L_x}{5U_B} . \quad (67)$$

Some specifications for the collector optics (telescope) follow from the tolerance column. The angle of view or pointing accuracy is given by the smallest value of $\Delta\alpha$ or $\Delta\beta$. The rotation rates required for stabilization of the telescope platform follow from the condition that the beam oscillation should be kept so small that it takes more than the sampling period, $\Delta\tau$, to produce an angular error of size

$$\frac{1}{10}\Delta\beta \text{ or } \frac{1}{10}\Delta\alpha$$

$$\dot{\Delta\alpha} \cong \frac{1}{10} \frac{\Delta\alpha}{\Delta\tau} \approx \cos^2\alpha \frac{\Delta h}{b} \frac{U_B}{L_x} . \quad (68)$$

$$\dot{\Delta\beta} \cong \frac{1}{10} \frac{\Delta\beta}{\Delta\tau} \approx \frac{2}{10} \frac{U_B}{b} . \quad (69)$$

Typical pointing and tracking accuracies have been calculated for orbital and ground-based detection (see table 6).

The above considerations are sufficient to outline telescope arrangements needed to scan a certain altitude from either the ground or orbit. However, the characteristics of the crossed-beam system in terms of the length, P, of the scanned portion, the number of photo-detectors, N, and the spatial and temporal resolutions of convection speeds, length scales, and wave number components cannot be determined without conducting several experiments.

Table 6

Pointing Accuracies and Stabilization of Telescope Platform

Pointing

$$\Delta\beta \cong \frac{2}{5} \frac{L_x}{b}; \quad \Delta\alpha \cong 2 \cos^2\alpha \frac{\Delta h}{b}.$$

Stabilization

$$\dot{\Delta\beta} \cong \frac{2U_B}{10b}; \quad \dot{\Delta\alpha} \cong \cos^2\alpha \frac{\Delta h U_B}{b L_x}.$$

Detector Position	Base-line [kms]	Turbulence Length Scale L_x [m]	Altitude Tolerance Δh [m]	Accuracy
ground ($U_B = 500$ m/sec)	10	100	50	$\Delta\alpha = \Delta\beta = 4 \times 10^{-3} =$ 15 arc min
				$\dot{\Delta\alpha} = \dot{\Delta\beta} = 10^{-2} \text{ sec}^{-1} =$ 34 arc min/sec
500 km orbit ($U_B = 8000$ m/sec)	1000	250	100	$\Delta\alpha = \Delta\beta = 10^{-4} = 0.34$ arc min
				$\dot{\Delta\alpha} = \dot{\Delta\beta} = 1.6 \cdot 10^{-4} \text{ sec}^{-1}$ 0.5 arc min/sec

Comment:

$$\alpha = \alpha_A = \alpha_B = \frac{1}{2} \alpha_{AB} = 45^\circ.$$

We plan to conduct several experiments in which the true range and resolution of scanning crossed-beam systems are established by comparing the optically measured convection speeds with horizontal wind measurements from meteorological towers and radiosondes. These experiments represent a step-by-step approach from simple space-fixed beams to rapidly scanning beams.

3. First Generation Experiments

The two sensors of the crossed-beam arrangement are placed on a short baseline with their intersection point set at a moderate height (about 25 m) above ground so that the results of the experiments can be compared to tower-mounted anemometers. The intersection points are fixed in height, but the beam separation distance is varied from 0 to 200 meters in a number of discrete steps. At each step the following results are obtained:

- (1) The rms intensity of the registered fluctuations.
- (2) The detector signal-to-noise ratio.
- (3) The horizontal wind speed, turbulent lengths, and wave length spectrum of the phenomena occurring in the region of beam crossing.
- (4) The spatial and temporal resolution of the system.
- (5) The effect, if any, of the beam diameter on the resolution of the system.

The first series of tests should serve to establish the soundness of the apparatus design. Once satisfactory results are obtained with this short range arrangement, the baseline of the detectors will be increased to approximately 20 km to produce intersection heights of up to 10 km. The beam intersection point will be adjusted to discrete altitudes above tower heights to assess (1) rms levels and frequency range of fluctuations, which originate at higher altitudes, (2) the influence of the variation of the beam intersection angle on the measured correlation values, and (3) the scale of statistically inhomogeneous fluctuations.

These experiments will sense phenomena over longer ranges and under conditions of reduced light intensity and tracer concentration and will therefore be a more severe test of the feasibility of the technique as applied to atmospheric phenomena. The beam separation distance, ξ , should be varied to approximately 600 meters (approximately twice the mean eddy sizes at an altitude of 10 km) and data will be obtained on the five parameters listed at the beginning of section VII.2.

The considerations of section V anticipate no signal detection problems up to about 15 km. If the measurements are to be extended to an altitude of 30 km, a point might be reached where either the tracers or the light intensity or both fall below the minimum value necessary for producing a detectable signal. Since the ozone concentration at a given height varies with weather conditions, only actual field experiments will define the height limitations of the system.

4. Second Generation Experiments

Once the feasibility of applying the crossed-beam technique to the measurement of atmospheric turbulence phenomena has been established by the series of tests using fixed beams, an attempt will be made to obtain continuous coverage of turbulence phenomena by scanning the beams over the region of interest.

The two beams will be scanned in elevation so that their intersection point will describe horizontal traces in the region of interest. The scanning should require less than 1.5 minutes so that the turbulence phenomena can be considered as frozen during the period of one scan.

The main point of interest in this series of tests will be to determine the effect of the scanning speed of the beams on the measured quantities. In particular, the replacement of time averages in a fixed spot with length average over the intersection path has to be tested. Certain types of inhomogeneous atmospheric turbulence are conceivable, where the average over one long path interval may have to be replaced with an ensemble average over many repeated sweeps of short length. The occurrence of such turbulent fields and the difference between a single sweep and multiple sweeps can be explored with rapidly scanning ground detectors. Multiple sweeps with orbiting detectors will not be possible.

A single sweep with two orbiting detectors will be sufficient, as long as the inhomogeneity is restricted to large scale phenomena. The inhomogeneity can then be removed as a nonstationary mean [23] or by employing structure functions [24]. Available experimental evidence [24] suggests that the suppression of nonstationary trends will be possible for most atmospheric applications of practical interest.

A second point of utmost practical importance is a decision whether an orbital sweep with two satellites could be replaced with the flight of a single satellite carrying two telescopes, A and B. The possibility of finding a crossing height by triangulation between the telescopes of a single satellite is provided by a time lag τ in the data reduction. This triangulation is illustrated in figure 22. The radiation sources which constitute the leading beam $B = A_j$ at time $t - \tau$ could be represented by an undelayed, imaginary satellite which is

trailing on the same orbit and possesses one telescope $A_i = B$. The line of sight of this delayed or imaginary beam $A_i = B$ intersects the undelayed beam A at an altitude which is given entirely by the time lag τ and the superposition of scanning and convective motions. Thus, altitude profiles can be measured by setting different time lags as discussed in section VI,4.

The sweep with a single satellite is possible whenever the atmospheric pattern remains frozen over the entire range of time lags. For $\alpha_A = \alpha_B = 1/2$ $\alpha_{AB} = 45^\circ$, the maximum time lag is identical to the time, $2b/U_B$, the satellite needs to travel twice the altitude. This lag is equal to $1000/8 = 125$ seconds. Many atmospheric patterns will be frozen over this time period. Therefore, a crossed-beam mission with two telescopes mounted on the same spacecraft appears feasible. The astronomical telescope (ATM), which is built by MSFC, would meet all the requirements outlined in this report and could thus be used for crossed-beam missions. The difference between astronomical observations and a crossed-beam experiment is that two telescopes are needed instead of one, and that a new mount is needed to point the telescopes downward instead of upward.

CONCLUSIONS

The ultimate objective of the flight experiment is to improve numerical methods for the prediction of weather, navigation and communication hazards, and pollution by providing the following data: (a) horizontal winds at global positions and altitudes which are requested by weather prediction centers and (b) turbulence spectra and scales showing the exchange of kinetic energy between large scale and small scale atmospheric motions. Other conceivable objectives, which are not treated in this report, would be (a) the early warning of clear-air turbulence by sweeping selected flight paths, and (b) waterbudget surveys employing a crossed-beam arrangement of millimeter wave detectors in this spectral region. All of these objectives may be met on earth orbital missions. If these missions should be successful, several generations of future missions become conceivable, which would monitor the ionosphere, the earth's magnetosphere, planetary atmospheres and the outer layers of the sun.

The crossed-beam method is a new test arrangement of two conventional remote sensing devices. Triangulation between the lines of sight of two radiation detectors is employed to select a local flow region which is centered around the line of minimum beam separation. Each of the two detectors will react to all emission, scattering, or

absorption processes inside its entire narrow field of view and the problem is thus to retrieve the local information from the region where the two beams cross. To do this the time history of the received radiative power of each beam is recorded and used as an input for statistical data reduction programs, which are commonly used in random vibration analysis and communication studies. The resulting time correlation between the two signals partially eliminates the integration over the optical path and retrieves the local information. The crossed-beam method works whenever detectable modifications of radiative power occur which are common to both lines of sight.

The crossed-beam concept has the following potential: (1) The art of remote sensing is extended to cover dynamic effects such as disturbances, turbulence, and wave-front phenomena in situations where other methods are restricted to single-point or single-path experiments and average over the optical path. (2) The method compares the fluctuations at the two points of minimum beam separation in a way required in the analytical description of random fields. (3) Crossed-beam spectroscopy should give the mean values of thermodynamic properties in inhomogeneous, turbulent, or unstable media which are not accessible to direct sensors. (4) A single sweep of frozen atmospheric patterns may establish the complete altitude profiles of turbulent intensity, turbulence length scales and wave member components. (5) The method is extremely versatile, since the tracking of man-made radiation sources is not necessary. A passive operation is possible using a natural radiation background. Furthermore, the entire electromagnetic spectrum from gamma rays to microwaves could be used.

The crossed-beam method has been experimentally verified in subsonic jets by comparing optically measured profiles of convection speeds, turbulence scales, space-time correlations and spectra with conventional hot-wire results [6]. Crossed-beam scanning over atmospheric distances has already been successfully demonstrated by measuring the height of the airglow phenomenon [2]. The crossed-beam method will work only if the following requirements are met:

(1) The atmospheric components of tracers must produce local changes in radiative power which are not lost during transmission to detector. In the atmosphere the mean radiative power is supplied by extended natural sources such as scattered sunlight and thermal emission. Inside the atmospheric window meteorological modulations occur, whenever a single beam sweeps over an inhomogeneous distribution of emission or extinction centers such as aerosols, ozone or water vapor.

(2) Light source fluctuations, shot noise, and instrument noise must be reduced to mean square levels which are not several orders of magnitude greater than the integrated signal. This is a far less restrictive requirement than the normal, which is that the erroneous noise should be at least one, and preferably two or three, orders of magnitude less than the genuine signal. The root mean square levels of the above meteorological fluctuations have been estimated and appear to be always larger than the noise levels of already available detectors such as the astronomical telescope (ATM).

(3) The lines of sight must intersect at or scan over a selected position for a sufficiently long integration period to pull the correlated signals out of the light source fluctuations, flow fluctuation, shot noise, and instrument noise. The necessary path length is intimately related to the magnitudes of the various noise contributions to the detected signals. Although, in principle, any degree of noise can be eliminated with suitable integration periods, the finite record lengths and the dynamic interchannel displacement set practical limitations to retrieving the local signal from the integrated signal and the combined light source noise, shot noise, and instrument noise. In a very rough estimate, a flight path interval of 15 km length has to be scanned with speeds in excess of 0.5 km/sec to measure horizontal wind and length scale profiles. Ground experiments are urgently needed to determine signals and noise for various "crossing heights."

On occasions the problems on meeting the above requirements will be formidable and may prohibit some of the desired applications. However, since we can pick the detected radiation from any region of the electromagnetic spectrum and since atmospheric applications allow large beam diameters and arbitrary orientations of the two lines of sight, we believe that there are many experiments where the above problems may be overcome, and useful, hitherto unavailable, data obtained.

The interpretation of the beam correlation (two-beam product mean value) is subject to the following theoretical restrictions.

(1) The number of statistically independent regions and gas dynamic phenomena is small enough to avoid cancellation of local fluctuations which would occur when integrating over too many statistically independent parts.

(2) Either emission or extinction dominates the local change of radiative power inside the correlation volume.

(3) The integrated fluctuation of the generalized extinction coefficient is sufficiently small to permit linearization. However, large changes in the mean value of the transmitted radiative power are permissible. Also, large local fluctuations are tolerable if one integrates over several statistically independent regions.

(4) The interpretation of a sweeping crossed-beam system is possible, if the region of interest is scanned rapidly enough to assume a frozen pattern and if the emission and/or extinction fluctuations are statistically homogeneous over the altitude tolerance or step which is desired in the altitude profile.

(5) The fluctuations of radiative power are locally isotropic over a "correlation disc." This assumption is sufficient, but violations are often tolerable. Crossed-beam experiments in anisotropic and inhomogeneous jet shear layers here already yielded a good approximation of two-point product mean values.

A step-by-step simulation of an in-flight experiment is outlined, which would allow one to assess the effect of the above practical limitations and theoretical restrictions. This is simulated by rotating two ground detectors in such a way that their intersection sweeps along a horizontal arc with orbital speed. Preliminary specifications for both ground and orbital detectors are given by relations, covering the lower limit, the upper limit and the tolerance of all independent test variables. It appears that crossed-beam missions could be accomplished with a single satellite, which carries two modified astronomical telescopes (ATM), which point toward the earth instead of away from the earth.

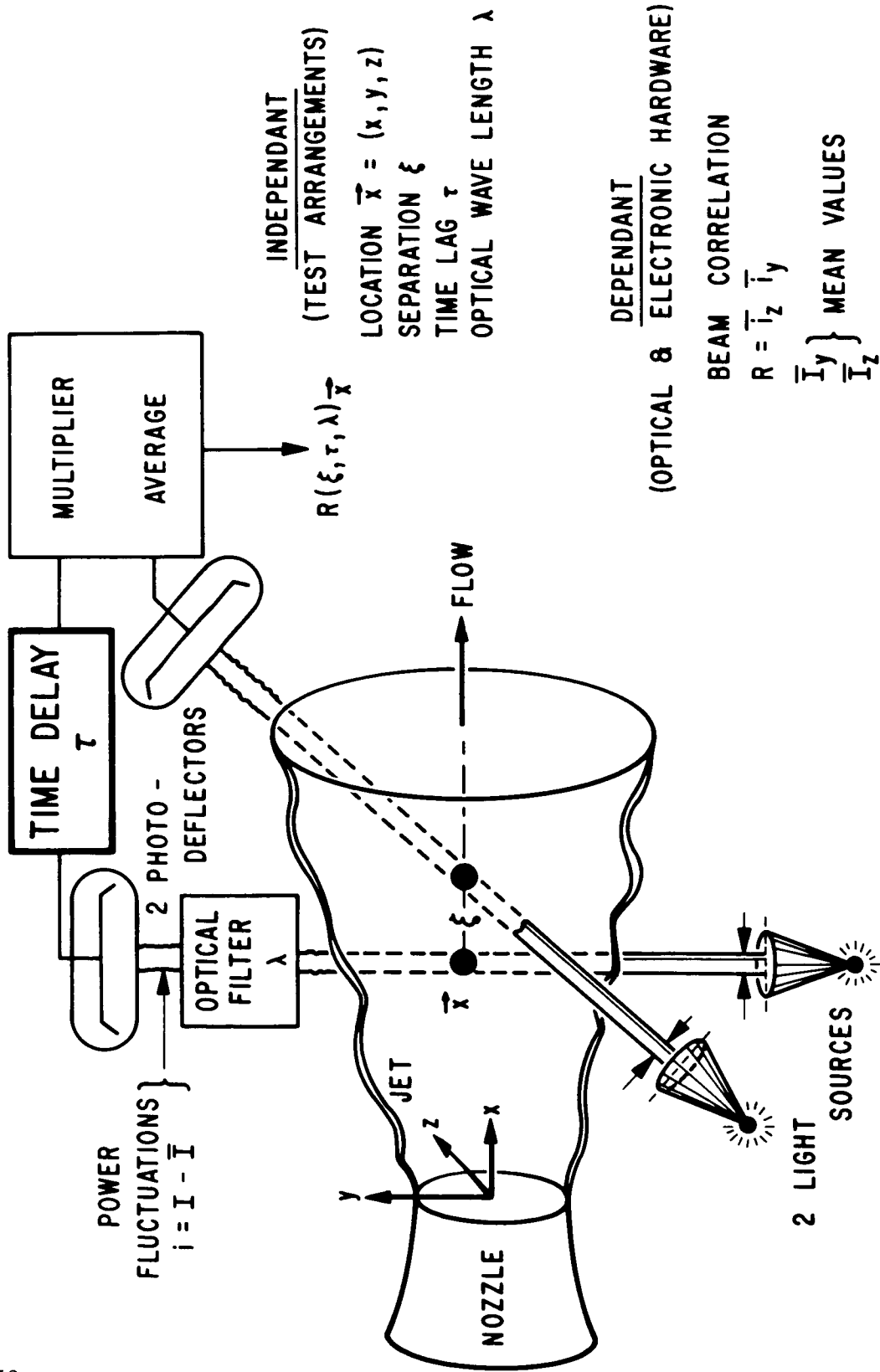


FIG. 1. SPACE FIXED CROSSED BEAM TEST ARRANGEMENTS

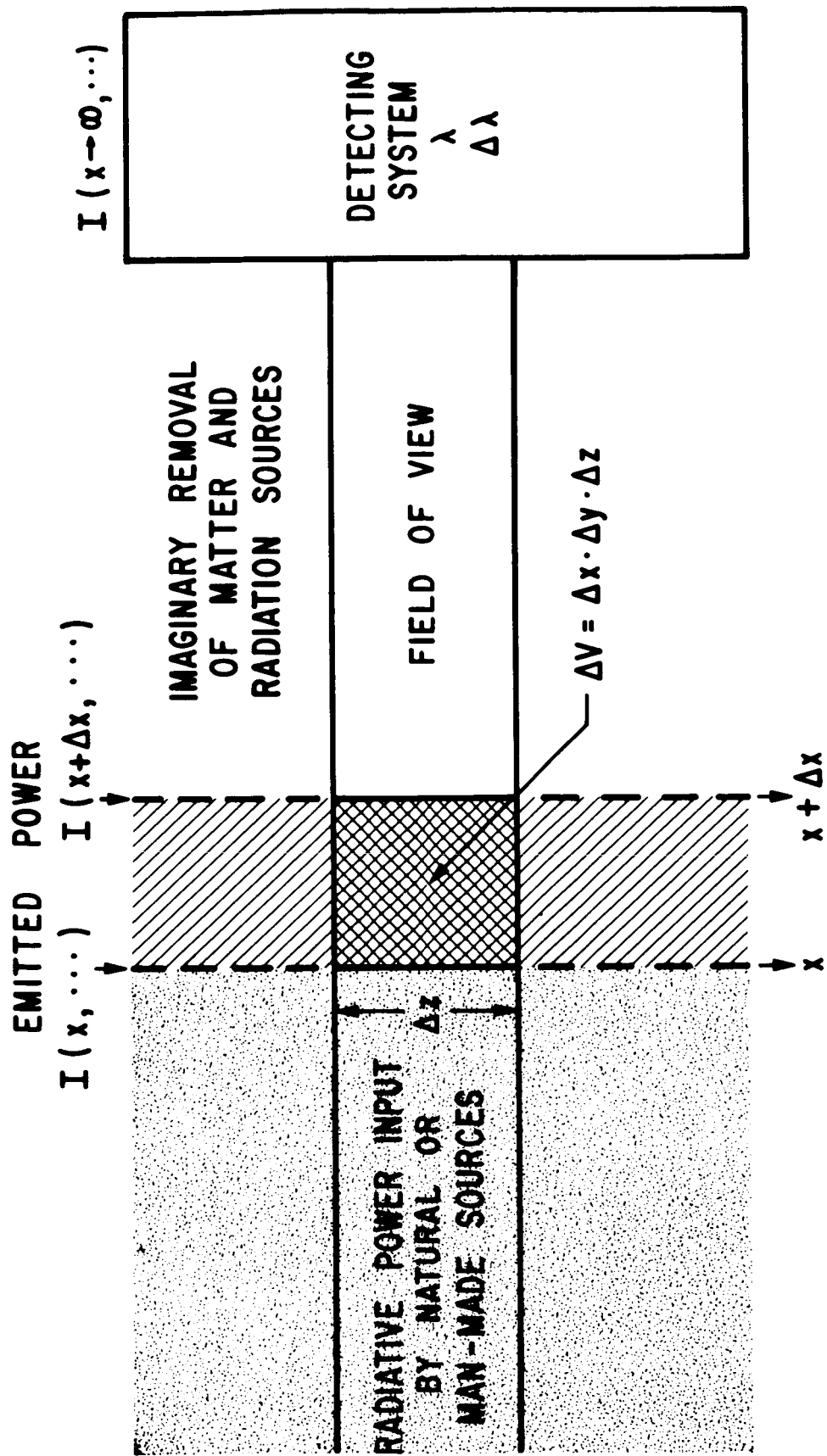
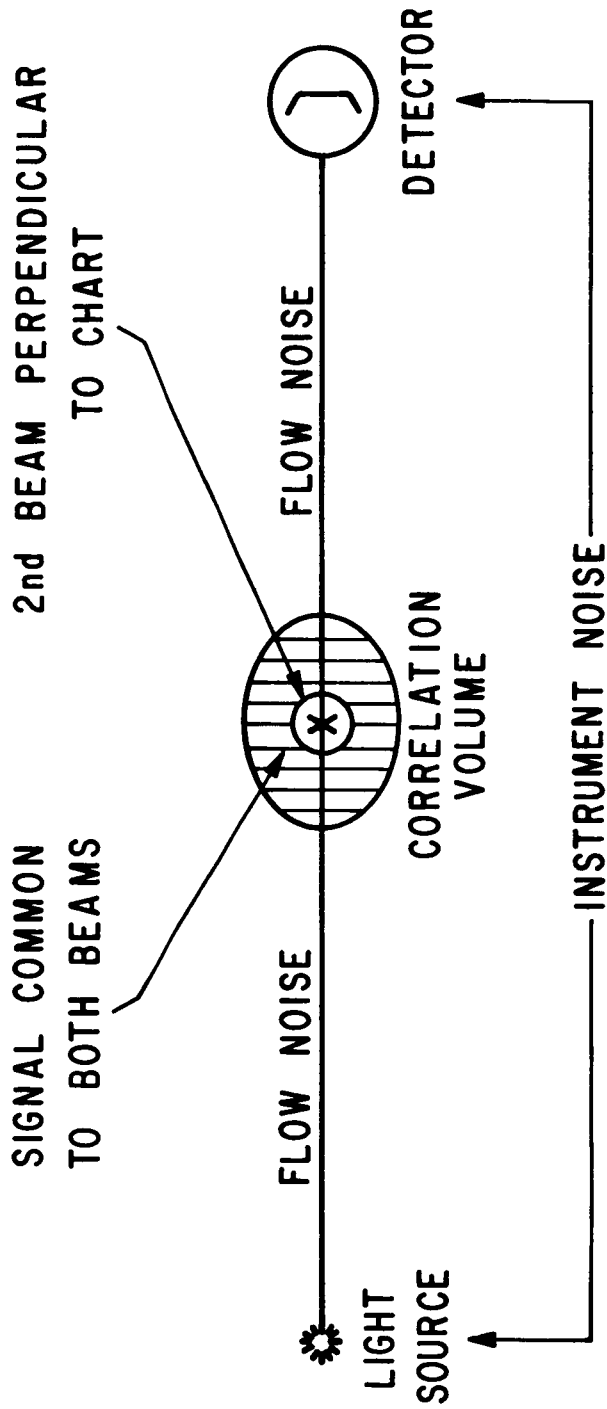


FIG. 2. REMOTE SENSING OF LOCAL CHANGES IN RADIATIVE POWER



CROSS CORRELATION ELIMINATES FLOW AND INSTRUMENT NOISE

FIG. 3. RETRIEVAL OF LOCAL INFORMATION

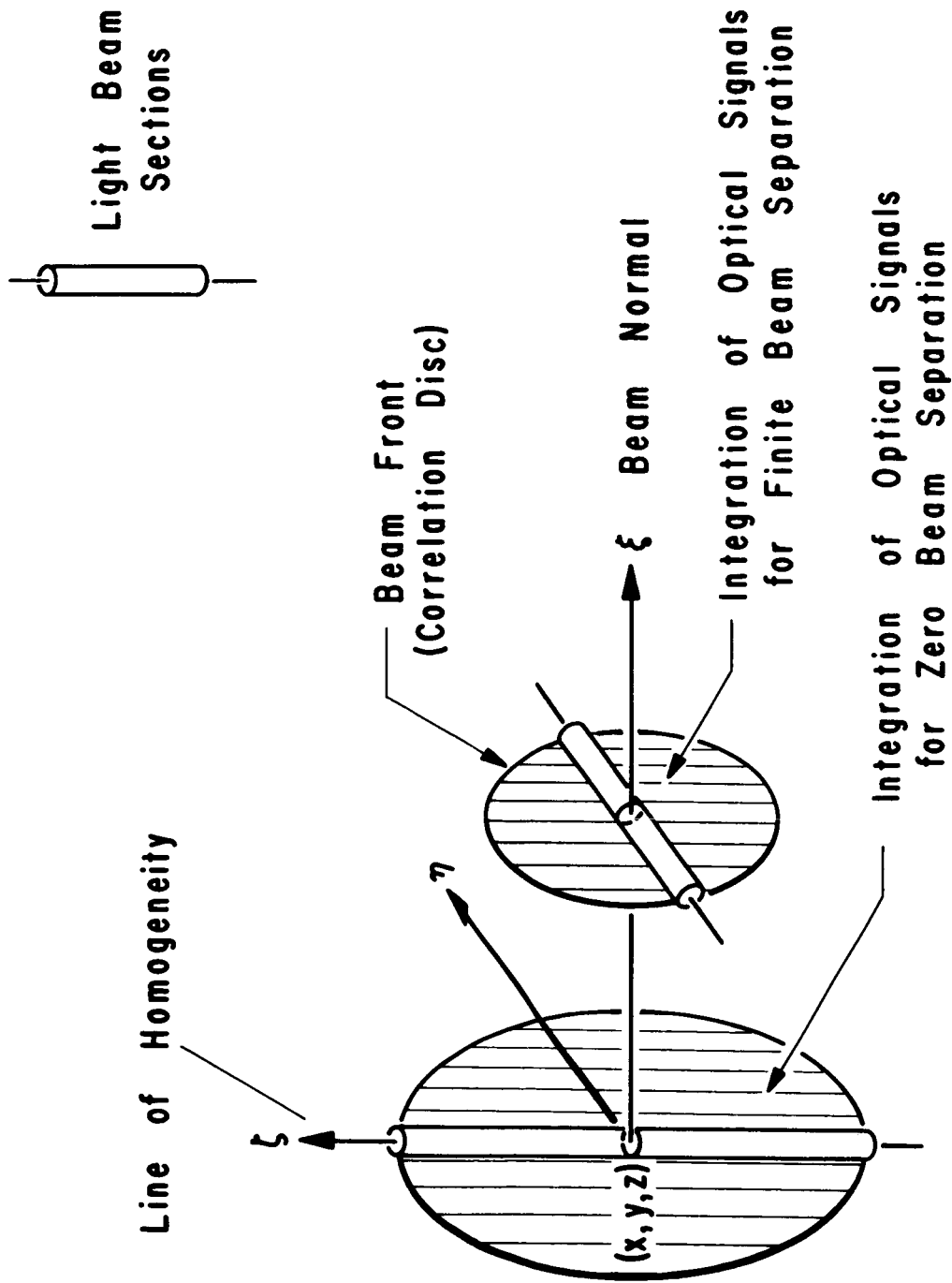


FIG. 4. OPTICAL INTEGRATION OVER CORRELATION AREAS (DISC)

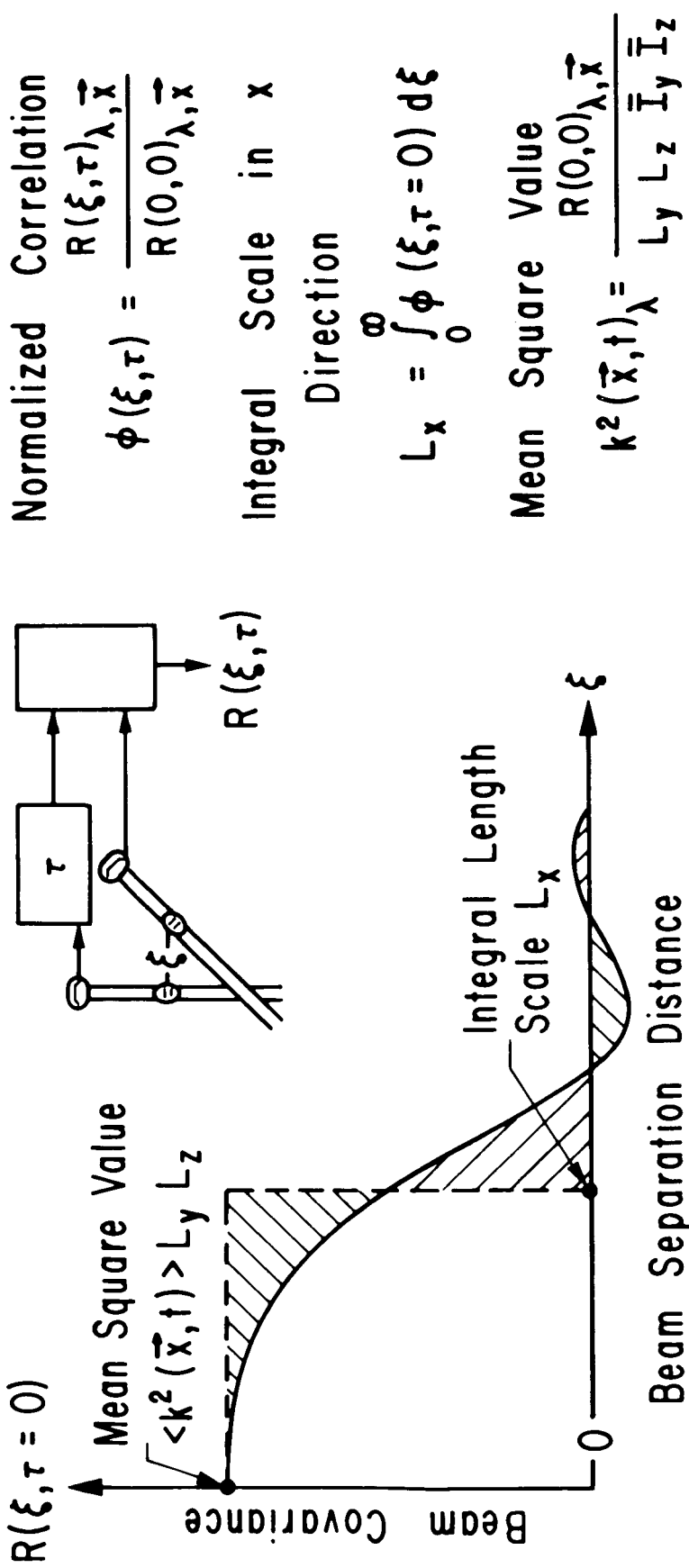
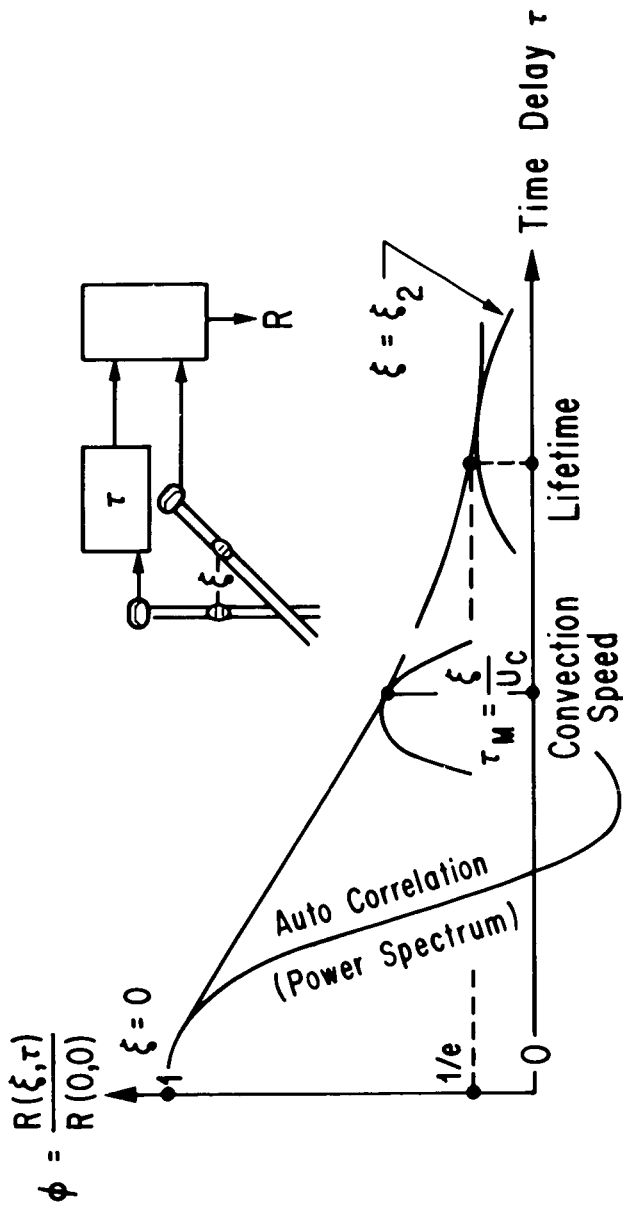


FIG. 5. EVALUATION OF SPACE CORRELATIONS



Read $\tau_M(\xi) \equiv$ Common Point of Individual $\phi(\tau)\xi$ and Envelope

Convection Speed $U_C = \xi / (\tau_M \xi)$

Moving Axis Auto Correlation $\phi^*[\tau = (\xi / U_C)] = \phi(\xi, \tau_M)$

Moving Axis Time Scale $L_\tau = \int_0^\infty \phi^*(\tau) d\tau$

Read Eddy Lifetime t_e from $\phi^*(\tau = t_e) = 1/e$

FIG. 6. EVALUATION OF TIME CORRELATIONS

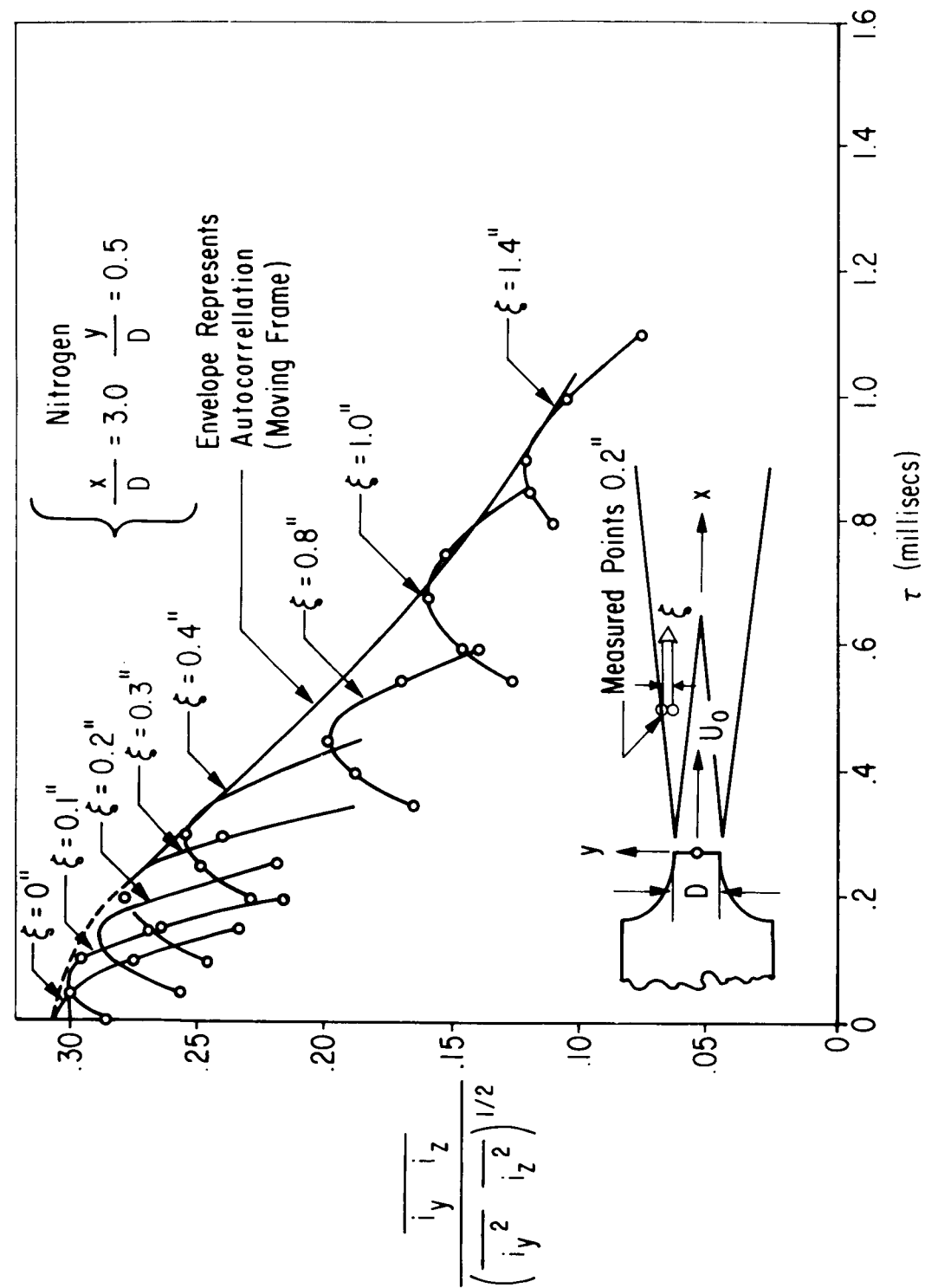


FIG. 7. CROSSED BEAM CORRELATION IN A SUBSONIC JET

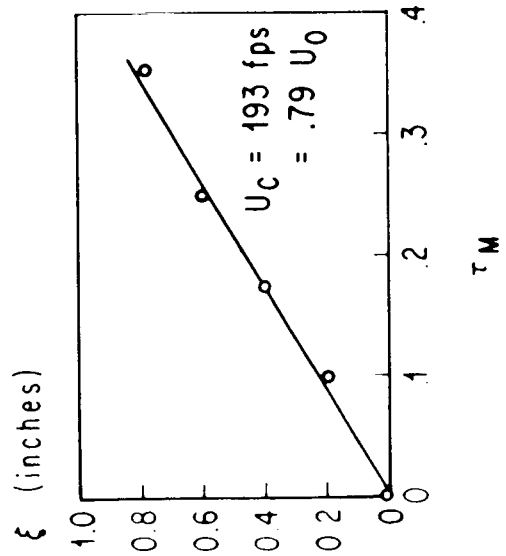
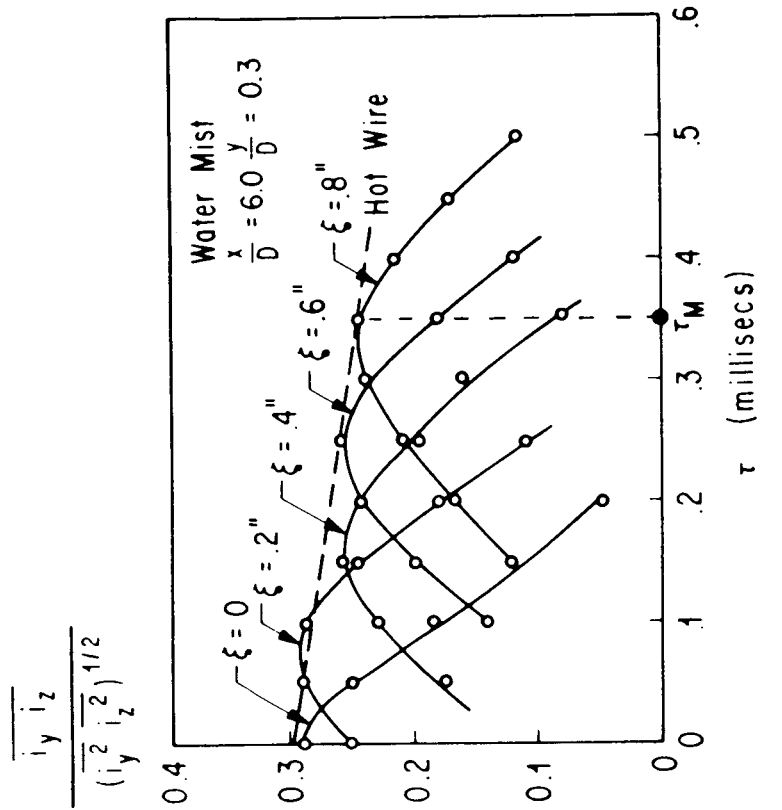
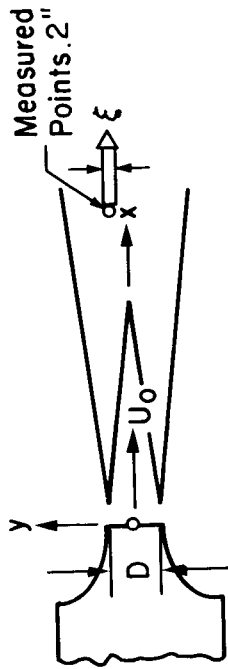


FIG. 8. TIME CORRELATIONS FROM CROSSED BEAM AND HOT WIRE MEASUREMENTS

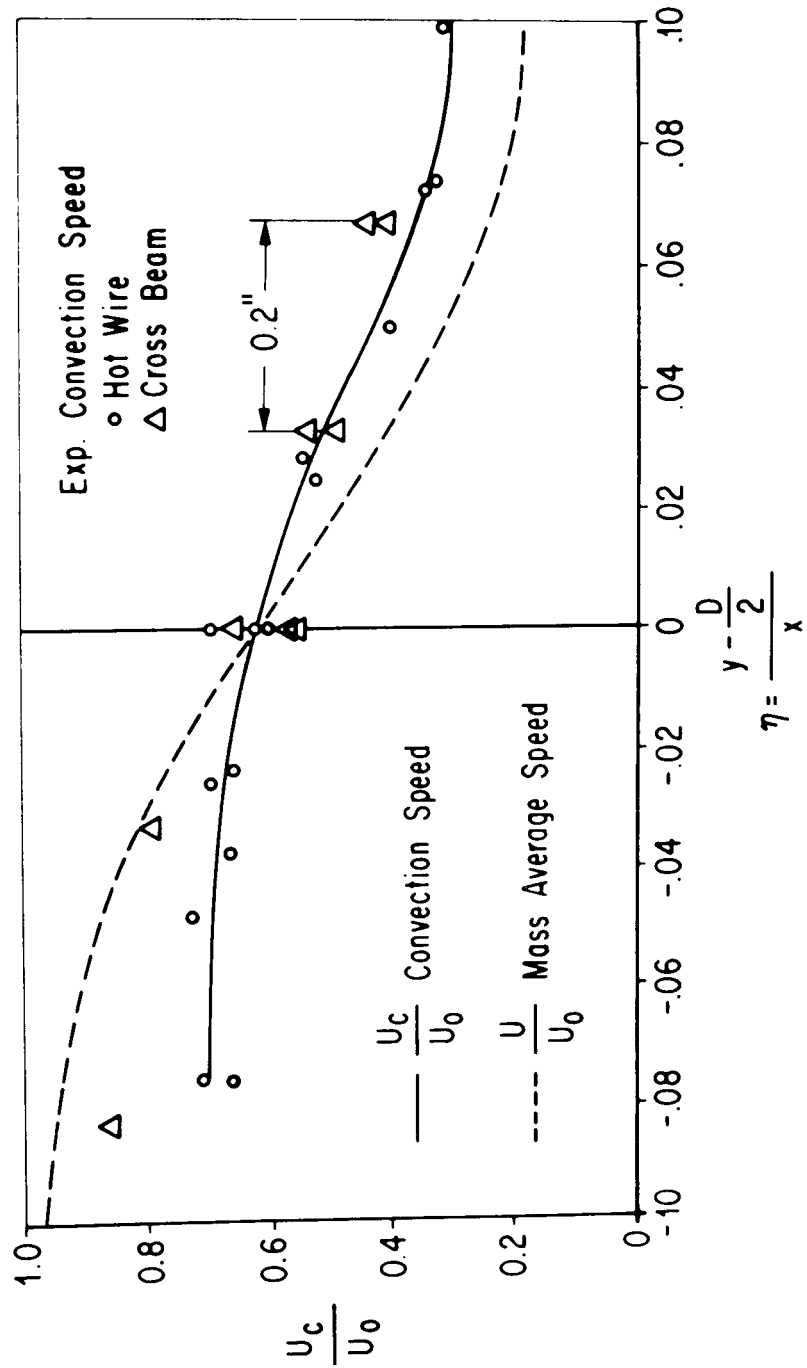
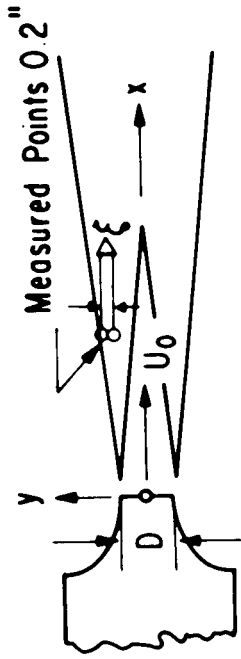


FIG. 9. VELOCITY PROFILES FROM HOT WIRE AND CROSSED BEAM METHODS

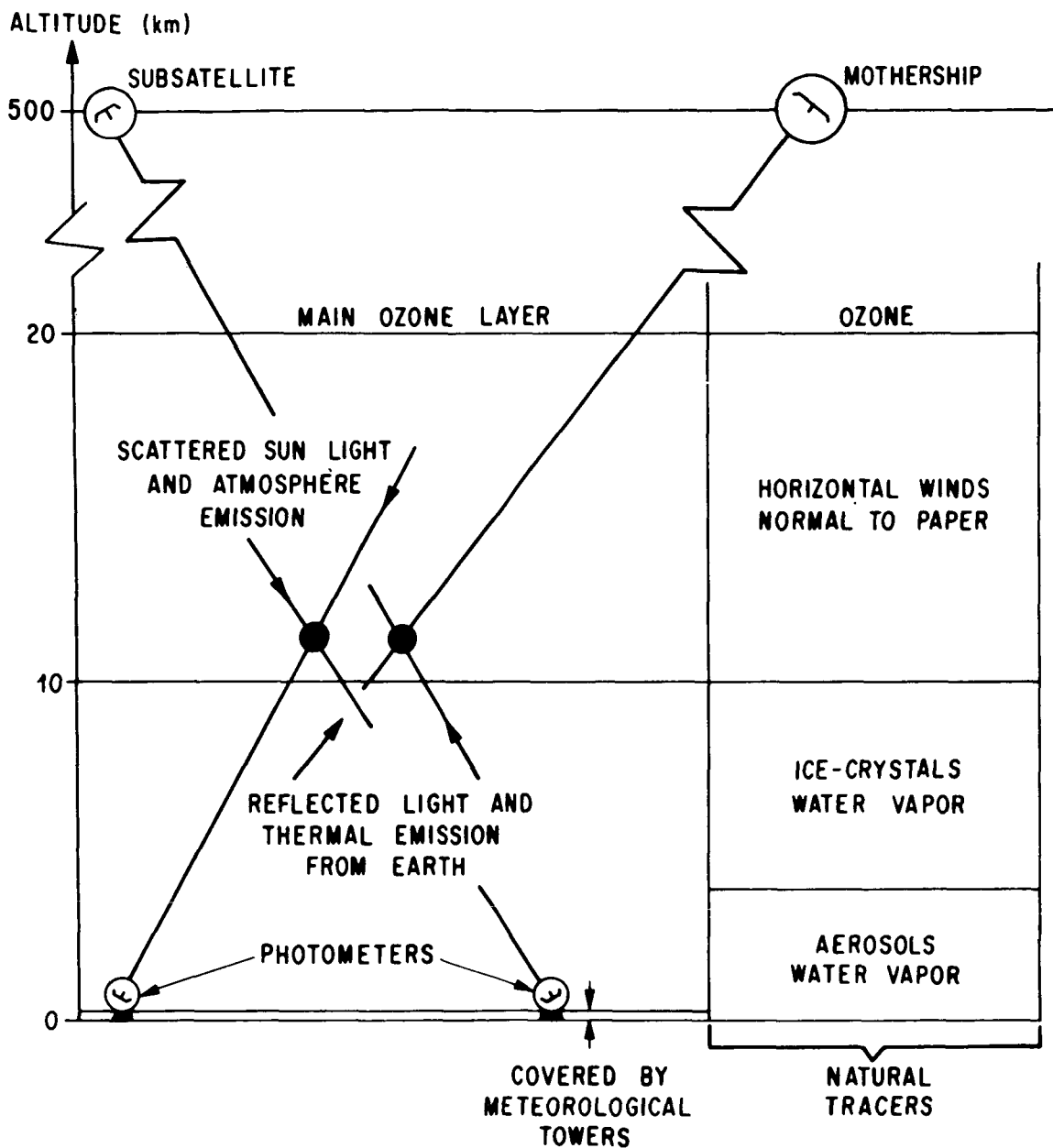


FIG. 10. CROSSED BEAM TEST ARRANGEMENTS FOR HORIZONTAL WIND MEASUREMENTS

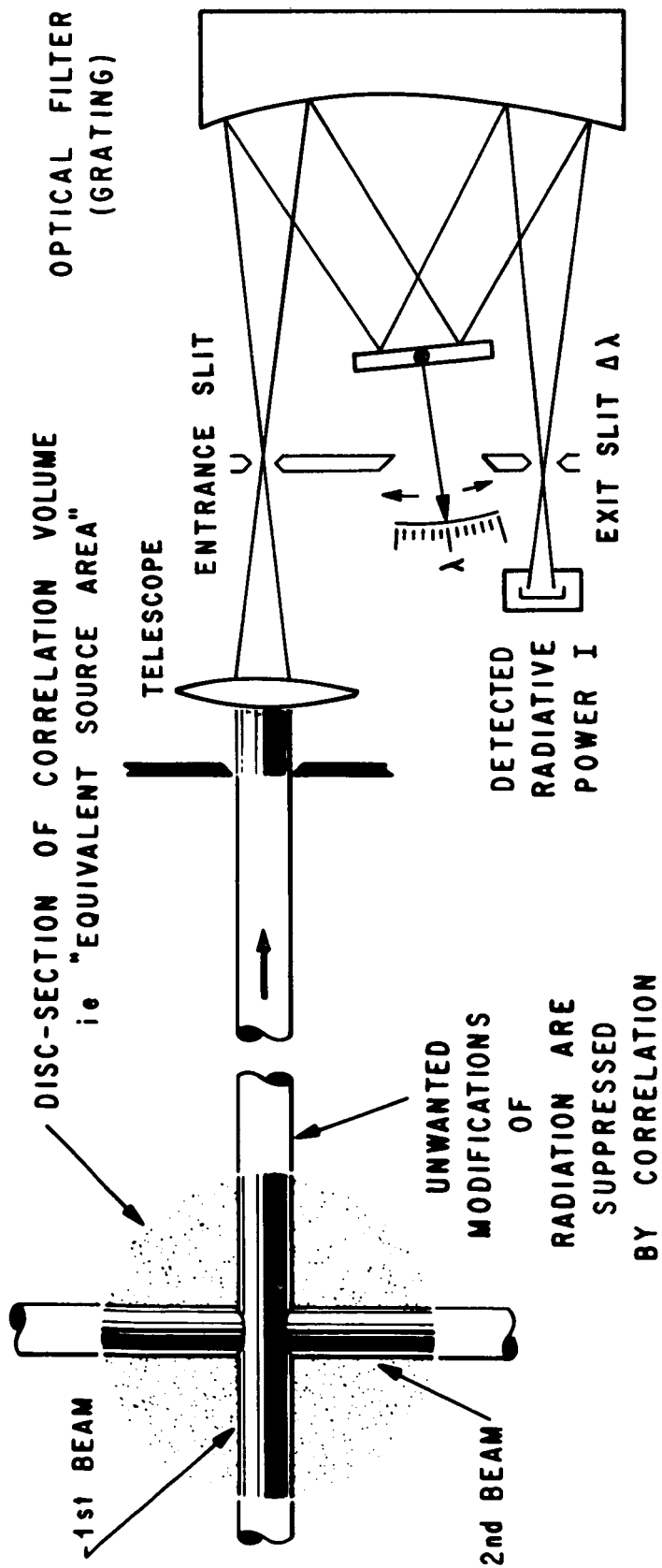


FIG. 11. CROSSED BEAM SPECTROSCOPY

APPROXIMATE LATITUDE	LOCATION	SCATTERED SOLAR RADIATION FLUX (10^{-3} WATTS/CM ²)			
		SUN ELEVATION ANGLE			
		10°	20°	30°	40°
60°	HELSINKI	3.5	4.9	6.3	7.0
50°	VIENNA	3.5	6.3	8.4	9.8
40°	NICE	--	7.0	8.4	9.1

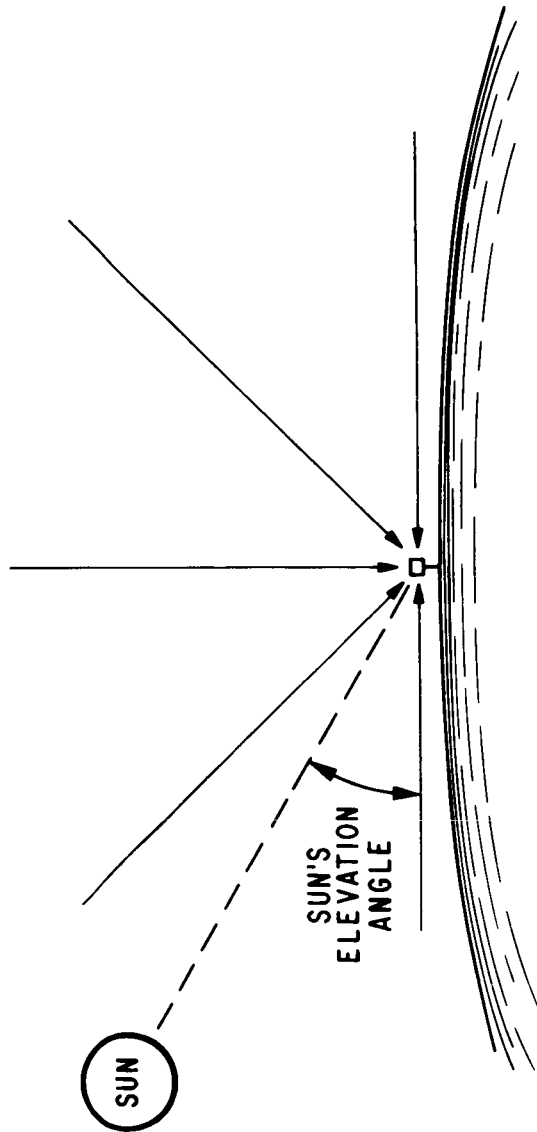
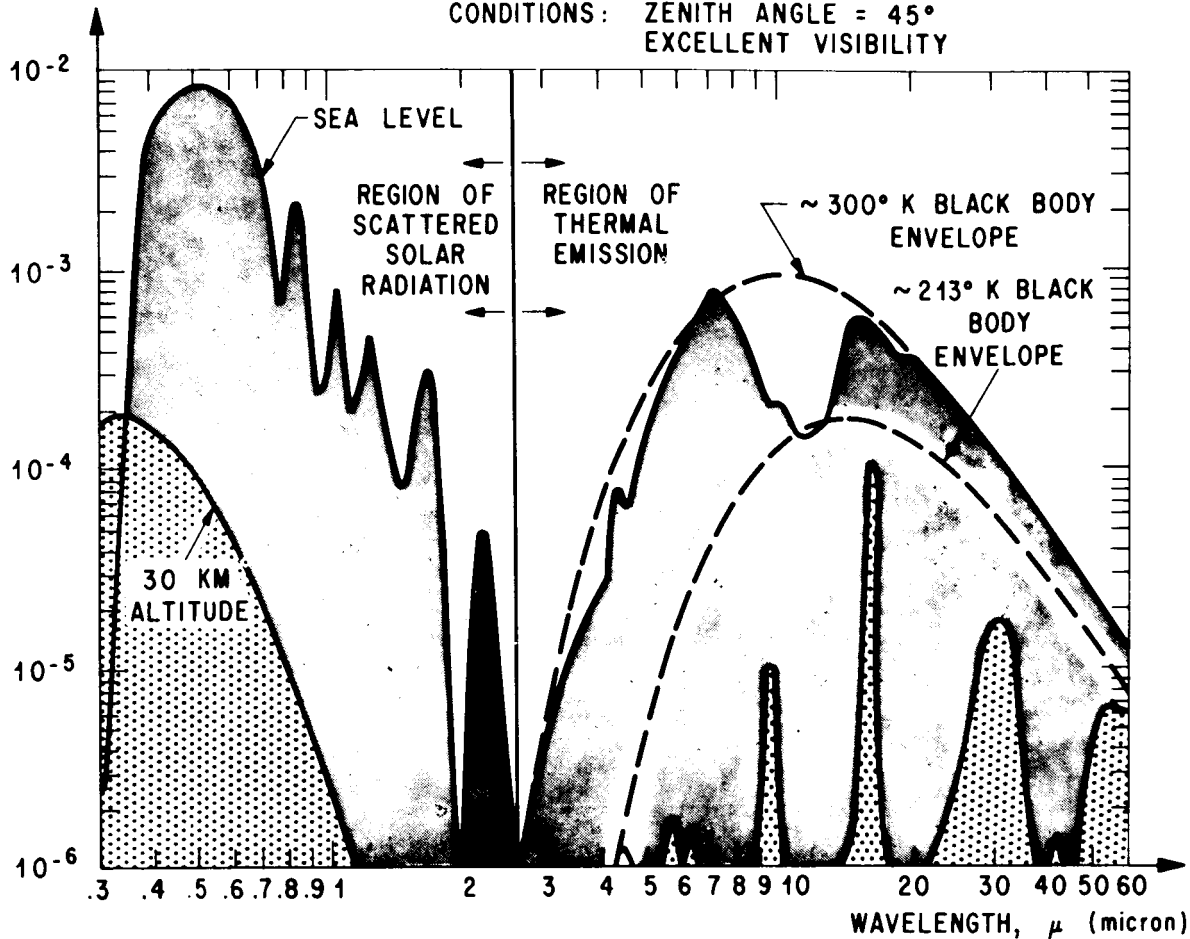


FIG. 12. DEPENDENCE OF SCATTERED SOLAR RADIATION ON LATITUDE AND SUN ELEVATION ANGLES

BACKGROUND RADIANCE, (watt/cm² micron ster)

CONDITIONS: ZENITH ANGLE = 45°
EXCELLENT VISIBILITY



TRANSMISSION RATIO

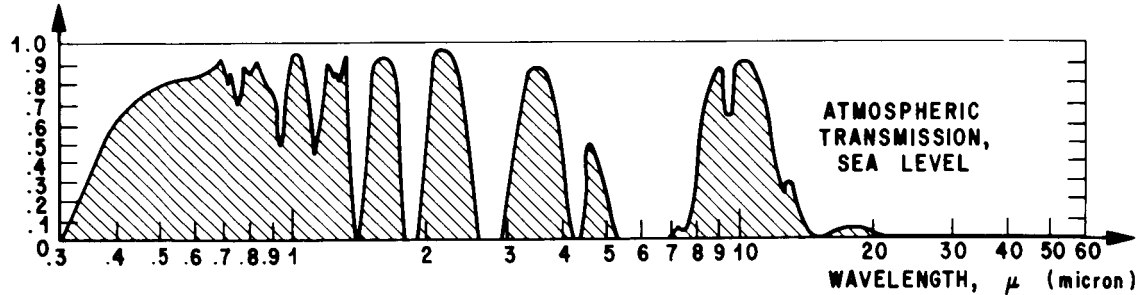


**FIG. 13. EMISSION SPECTRUM
OF ATMOSPHERIC RADIATION BACKGROUND
FOR TWO ALTITUDES (15)**

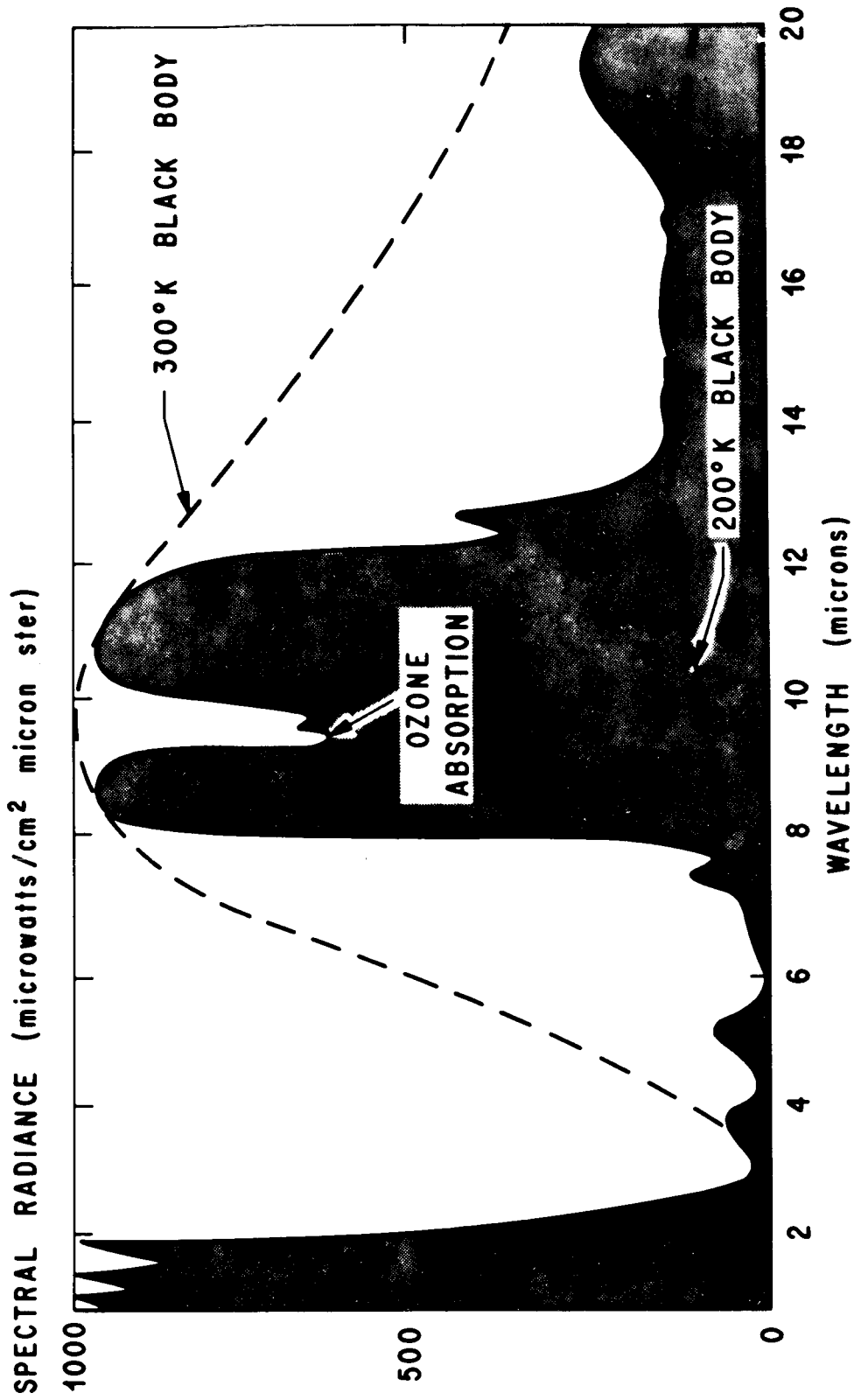


FIG. 14. SPECTRAL RADIANCE OF THE SUNLIT SIDE OF EARTH AS OBSERVED FROM A SATELLITE

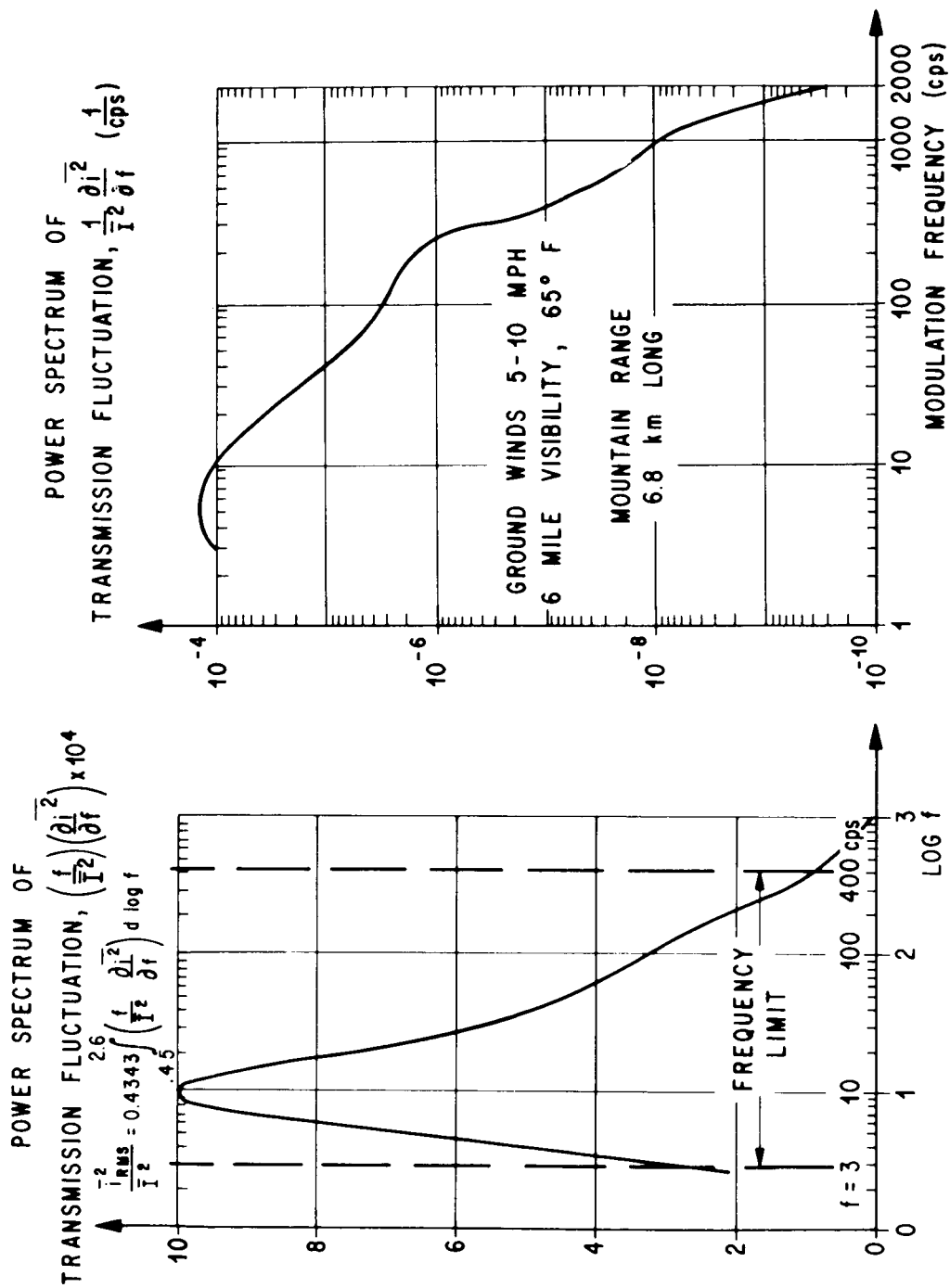


FIG. 15. ATMOSPHERIC MODULATION OF A LASER BEAM

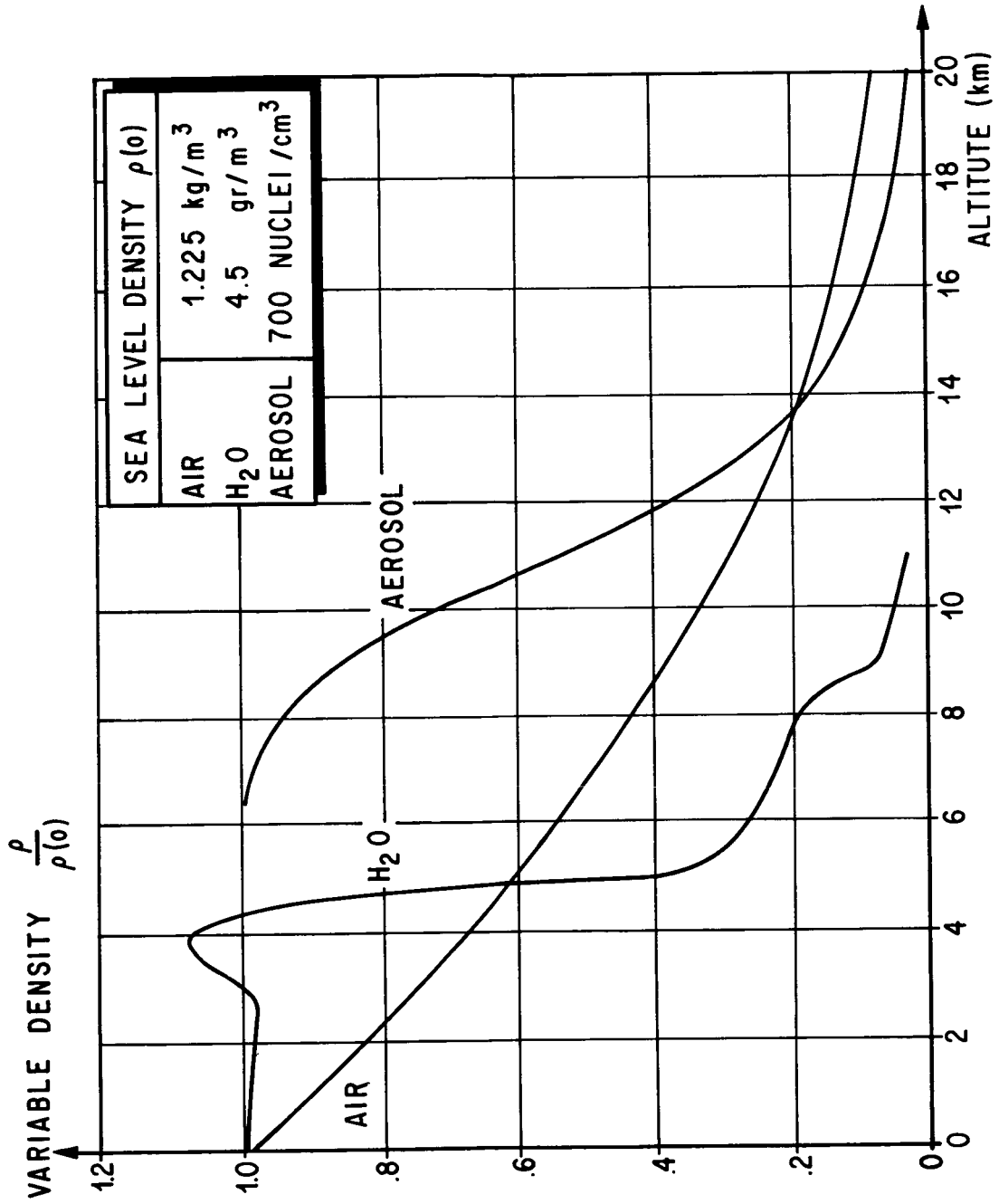
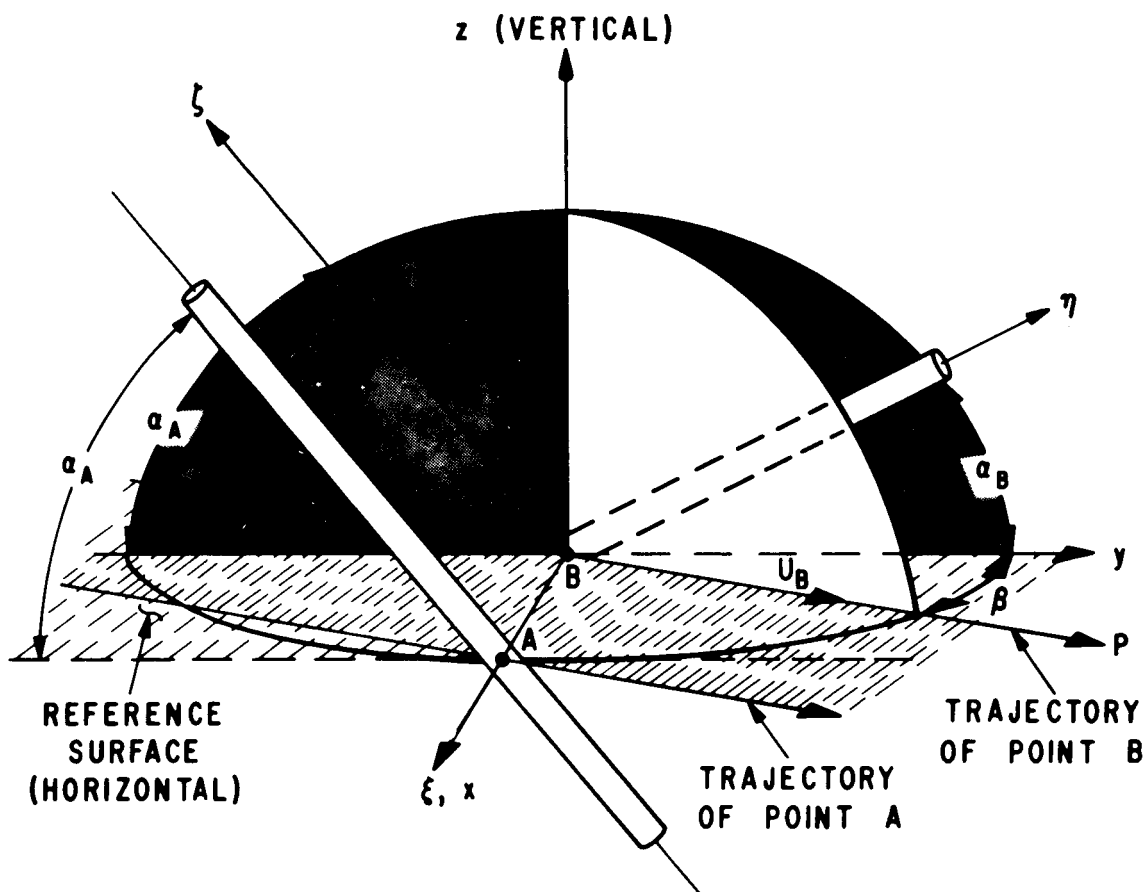


FIG. 16. TRACER AND AIR DENSITY DISTRIBUTION WITH HEIGHT



x, y, z , ATMOSPHERE FIXED COORDINATES
 ξ, η, ζ , BEAM FIXED COORDINATES

THE NORMAL ξ SWEEPS OUT THE HORIZONTAL x, y PLANE

FIG. 17. TRANSLATION OF A RIGID CROSSED
 BEAM ARRANGEMENT

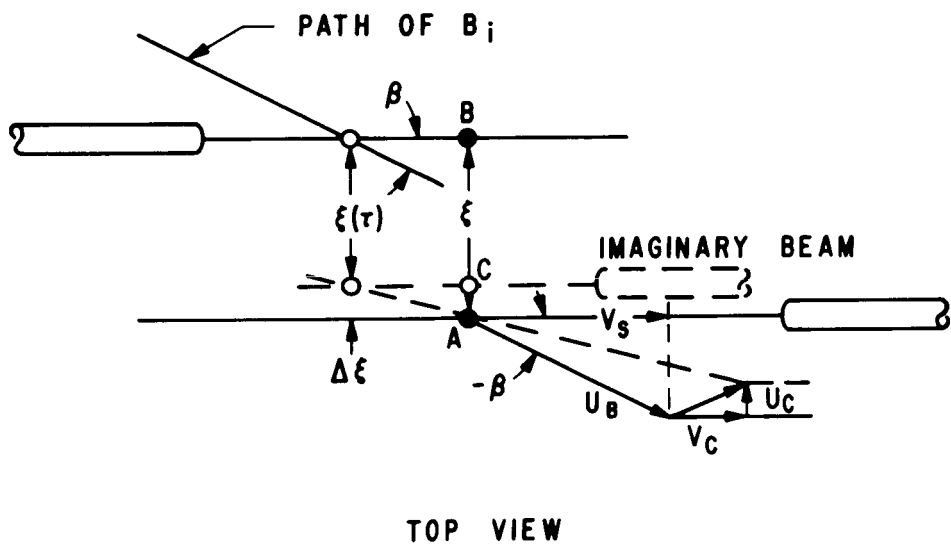
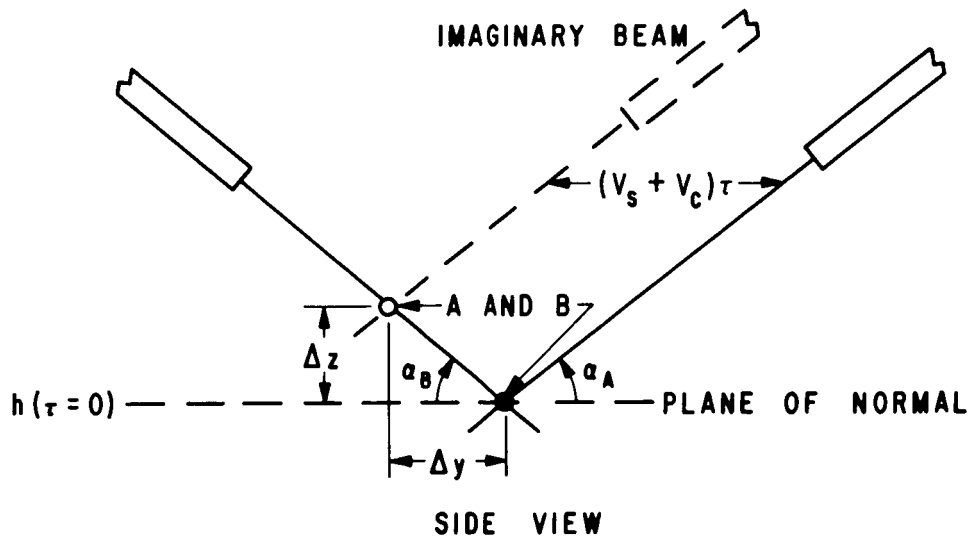
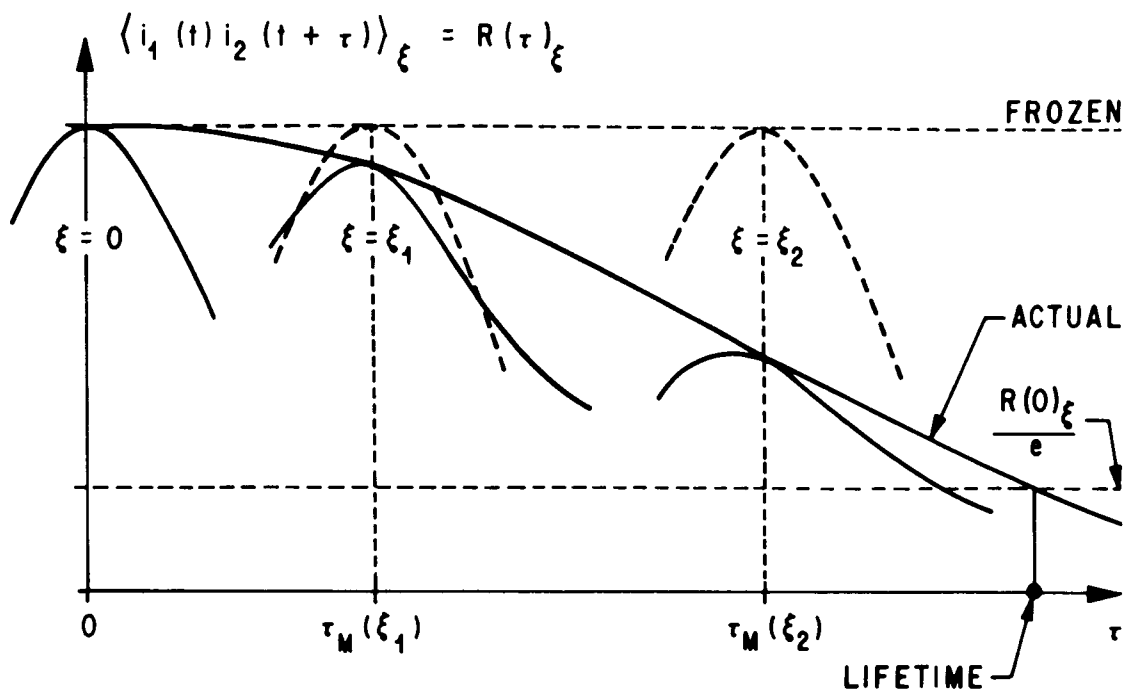


FIG. 18. POINTS OF MINIMUM SEPARATION A_i AND B_i BETWEEN IMAGINARY AND UNDELAYED BEAM



— ACTUAL CORRELATION
 ---- EXPECTED FOR FROZEN PATTERNS

GROUP VELOCITY FOLLOWS FROM POSITION OF MAXIMUM :

$$U_c = \frac{\xi}{C_{AB} \tau_M(\xi)} - U_B \sin \beta$$

FIG. 19. GROUP VELOCITY MEASUREMENT WITH SCANNING BEAMS

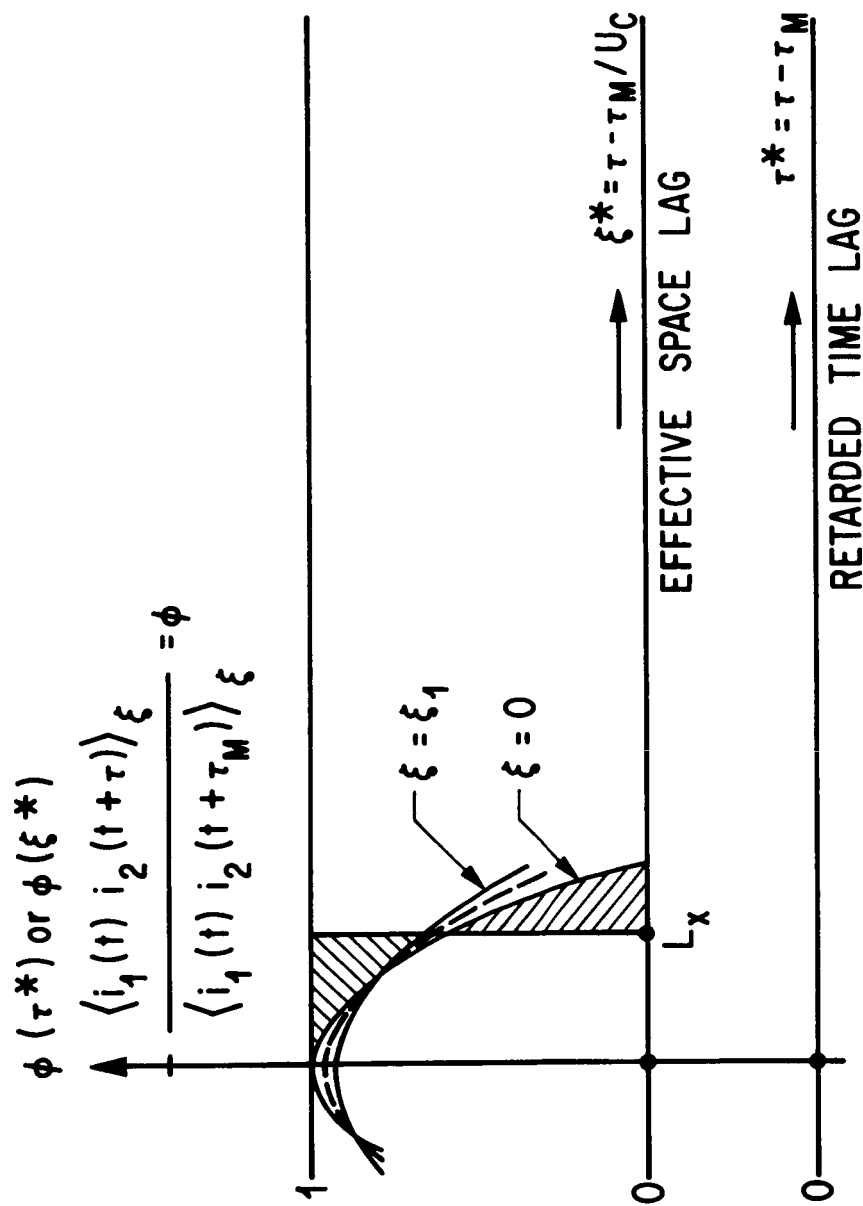


FIG. 20. ESTIMATE OF NORMALIZED AUTOCORRELATION AND SPACE CORRELATION FUNCTIONS

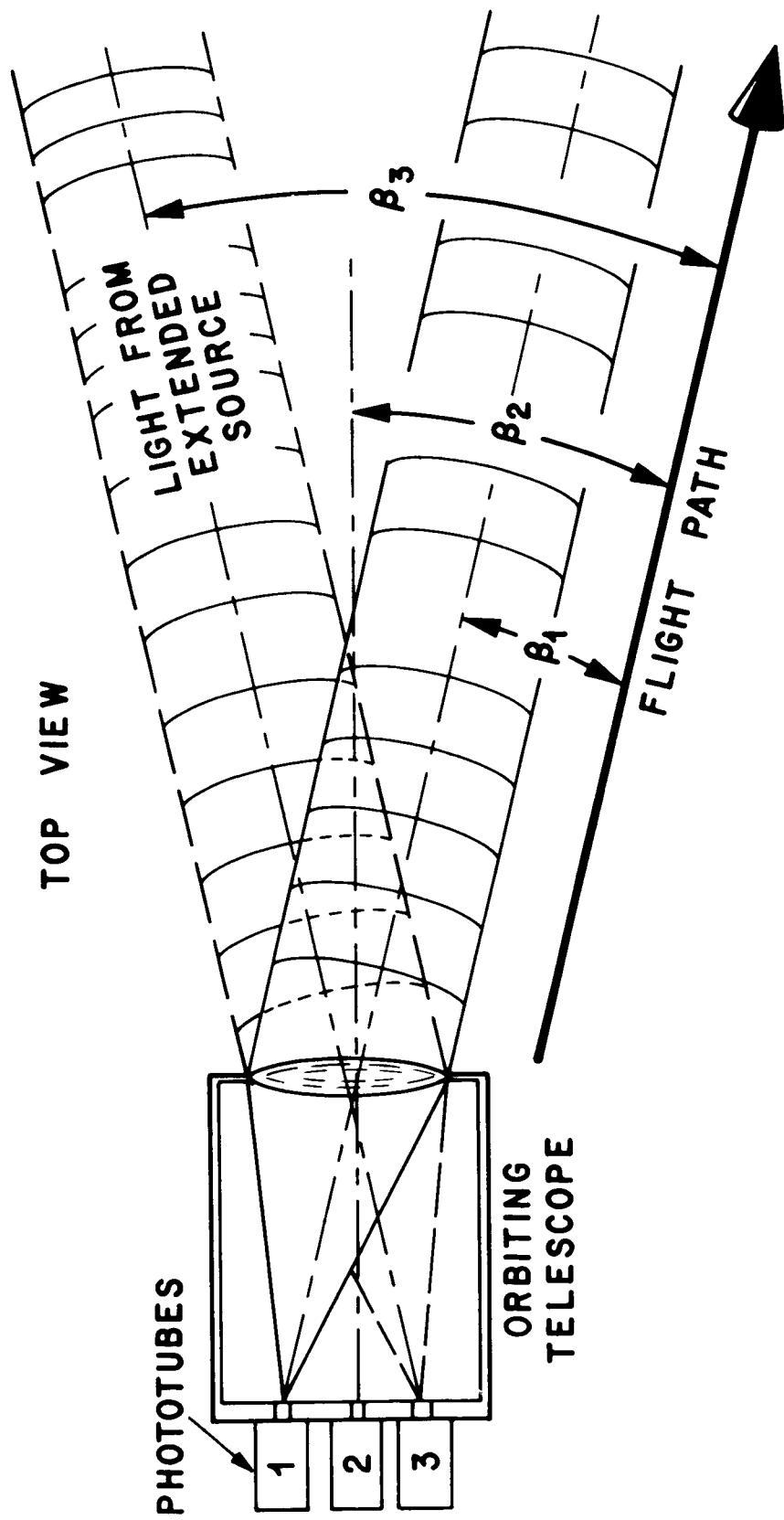


FIG. 21. PHOTO DETECTOR ASSEMBLY FOR SWEEPING ALTITUDE PROFILES

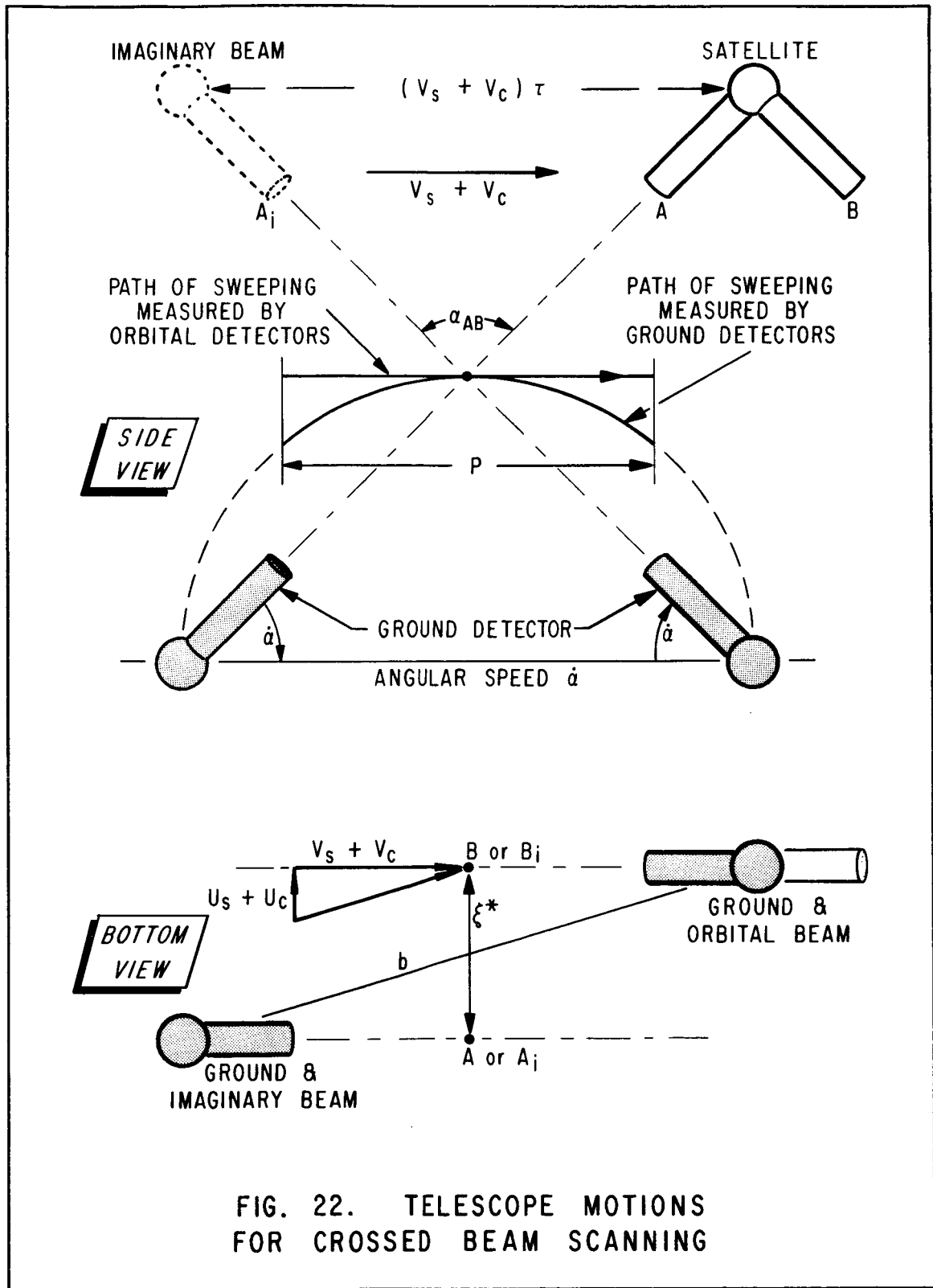


FIG. 22. TELESCOPE MOTIONS FOR CROSSED BEAM SCANNING

REFERENCES

1. Fisher, M. J. and F. Krause, "Local Measurements in Turbulent Flows Through Cross-Correlation of Optical Signals," NASA TM X-53295, April 1965, pp. 66-75.
2. Wolff, M. M., "A New Attack on Height Measurement of the Nightglow by Ground Triangulation," *Journal Geoph. Res.*, Vol. 71 (1966), pp. 2743-2748.
3. Krause, F. R. and M. J. Fisher, "Remote Sensing of Local Flow in Stabilities and Turbulence," ASME Flow Measurement Symposium, Pittsburg, September 26-28, 1966, pp. 171-194.
4. R. W. Pohl, Standard Text on Equations of Radiative Transfer, Springer (1963), Berlin, ed. 11.
5. Batchelor, K. G., The Theory of Homogeneous Turbulence, Students ed., Cambridge Univ. Press, 1960.
6. Fisher, M. J. and F. Krause, "The Crossed-Beam Correlation Method," *J. Fluid Mech.*, accepted for publication in 1967.
7. Davies, P. O. A. L., M. J. Fisher and M. O. Borrat, "The Characteristics of Turbulence in the Mixing Region of a Round Jet," *J. Fluid Mech.*, Vol. 15 (1962), pp. 337-367.
8. Hinze, J. O., Turbulence, McGraw-Hill Book Co., New York, 1959.
9. Fisher, M. J. and P. O. A. L. Davies, "Correlation Measurements in a Non-Proven Pattern of Turbulence," *Fluid Mechanics*, Vol. 18, pp. 97-116, 1964.
10. Lin, C. C., "Statistical Theories of Turbulence," Princeton Univ. Press, 1961.
11. Wills, J. A. A., "On Convection Velocities in Turbulent Shear Flows," NPL-Aero Report 1050 (1963).
12. Davies, P. O. A. L., "The Near Field Generated by Intense Turbulence," Paper L53, Proc. 5th International Congress on Acoustics, Liege, Belgium, September 1965.
13. Fisher, M. J., "Optical Measurements with a High Temporal and Spatial Resolution," IITRI Progress Report M6114-23, Contract NAS-11258, May 9, 1966.

REFERENCES (Continued)

14. Krause, F. R., J. G. La France, S. V. Paranjape, and J. B. Stephens, "Feasibility and Potential of Atmospheric Crossed-Beam Experiments," NASA-MSFC, Aero-Astrodynamic Research Review No. 5, to be published.
15. Project Mesa, "Present and Future Air Force Needs for Environmental Measurements," Geophysics Corporation of America, January 1962.
16. Johnson, D. S., Statement before the Senate Aeronautical and Space Science Committee, March 12, 1965. Bull. Am. Meteorol. Soc., Vol. 46, 1965, pp. 200-202.
17. Kondrat'yev, K. Y., "Actinometry," NASA TT F-9712.
18. Goody, R. M., W. T. Roach, "Determination of the Vertical Distribution of Ozone from Emission Spectra," Quarterly Journal of the Royal Meteorological Society (1956) 82-217-221.
19. Coulson, K. L., J. V. Dave, and Z. Sekera, "Tables Relating to Radiation Emerging from a Planetary Atmosphere with Rayleigh Scattering," Univ. of Calif. Press (1960).
20. IIT Staff, "Coherent Optical Propagation Study," RADC-TR-65313, November 1965.
21. Burns, A. and C. K. Rider, "Project Topcat, Power Spectral Measurements of Clear Air Turbulence Associated with Jet Streams," Royal Aircraft Establishment Technical Memo, 1965.
22. Montgomery, A. J., et al., IIT Research Institute Supplementary Reports under Contract No. NAS8-20107.
23. Krause F. R., J. A. Jones, M. J. Fisher, "Digital Analysis of Random Processes by Piecewise Estimated Correlation Functions," Preliminary Report, R-AERO-AM, July 1966, to be published as NASA-TN.
24. Tatarski, V. I., Wave Propagation in a Turbulent Medium, McGraw-Hill, 1961.
25. Bendat, J. S. and A. G. Piersol, Measurement and Analysis of Random Data, John Wiley & Sons, Inc., New York, 1966.

APPENDIX A

Approximation of Point Correlations in Locally Isotropic Fields

The three dimensional wave number components S_k of the scalar k field [8] can be expressed by the experimentally accessible two-beam product mean value R by using equation (17).

$$\begin{aligned}
 S_k(\psi_1; \psi_2 = 0; \psi_3 = 0, \tau) &= \frac{1}{8\pi^3} \int_{-\infty}^{+\infty} \int_{-\infty}^{+\infty} \int_{-\infty}^{+\infty} R_k(\vec{\xi}, \tau) e^{i\vec{\xi} \cdot \vec{\psi}} d\vec{\xi} \\
 &= \frac{1}{8\pi^3} \int_{-\infty}^{+\infty} e^{-i\xi\psi_1} \left(\int_{-\infty}^{+\infty} \int_{-\infty}^{+\infty} R_k(\vec{\xi}, \tau) d\eta d\xi \right) d\xi \\
 &= \frac{1}{8\pi^3} \int_{-\infty}^{+\infty} e^{-i\xi_1\psi_1} \frac{R(\xi_1; \tau)}{\bar{I}_y \bar{I}_z} d\xi_1. \tag{A1}
 \end{aligned}$$

S_k is also indirectly related to the desired two-point product mean value by an inverse Fourier transformation

$$R_k(\xi, \eta = 0, \zeta = 0, \tau) = \int_{-\infty}^{+\infty} \int_{-\infty}^{+\infty} \int_{-\infty}^{+\infty} S_k(\psi_1; 0; 0, \tau) e^{+i\psi_1\xi} d\vec{\psi}. \tag{A2}$$

For isotropic turbulence, the wave number components S_k are constant inside a spherical shell in the wave number space $\vec{\psi} = (\psi_1, \psi_2, \psi_3)$ where the volume of the shell is $4\pi \psi_1^2 d\psi_1$ and the value of S_k inside the shell is $S_k(\psi_1, 0, 0, \tau)$. Thus, the inverse Fourier transform may be expressed in the form

$$R_k(\xi, 0, 0, \tau) = \int_0^{\infty} S_k(\psi_1, 0, 0, \tau) e^{i\psi_1\xi} 4\pi \psi_1^2 d\psi_1. \tag{A3}$$

Substituting equation (A2) into (A3) and inverting the order of integration gives the desired relation between the two point product mean values R_k and the two beam product mean value R .

$$R_k(\xi, 0, 0, \tau) = \frac{1}{2\pi^2} \int_0^\infty \psi_1^2 e^{i\psi_1 \xi} \left\{ \int_{-\infty}^\infty e^{-i\psi_1 \xi_1} \frac{R(\xi_1, \tau)}{\bar{I}_y \bar{I}_z} d\xi_1 \right\} d\psi_1 \quad (A4)$$

$$R_k(\xi, 0, 0, \tau) = \frac{1}{2\pi^2} \int_{-\infty}^\infty \int_0^\infty \frac{R(\xi_1, \tau)}{\bar{I}_z \bar{I}_y} \psi_1^2 e^{i\psi_1(\xi - \xi_1)} d\psi_1 d\xi_1 .$$

This equation can be simplified by noting that the integral can be expressed by the derivative of another double integral,

$$R_k = - \frac{\partial^2}{\partial \xi^2} \left\{ \frac{1}{2\pi^2} \int_{-\infty}^\infty \frac{R(\xi_1, \tau)}{\bar{I}_z \bar{I}_y} \left[\int_0^\infty e^{i\psi_1(\xi - \xi_1)} d\psi_1 \right] d\xi_1 \right\} , \quad (A5)$$

the inner integral of which is proportional to the Dirac Delta Function [25].

$$\begin{aligned} \delta(\xi - \xi_1) &= 2\pi \int_{-\infty}^\infty e^{-i\psi_1(\xi - \xi_1)} d\psi_1 \\ &= -2\pi \left(\int_{-\infty}^0 e^{i\psi_1(\xi - \xi_1)} d\psi_1 + \int_0^\infty e^{i\psi_1(\xi - \xi_1)} d\psi_1 \right) \\ &= -4\pi \int_0^\infty e^{i\psi_1(\xi - \xi_1)} d\psi_1 . \end{aligned} \quad (A6)$$

Substituting (A6) into (A5) gives the final and simple result, which was quoted in section III, 2.

$$R_k(\xi, 0, 0, \tau) = \frac{1}{8\pi^3} \frac{\partial^2}{\partial \xi^2} \left\{ \int_{-\infty}^\infty \frac{R(\xi_1, \tau)}{\bar{I}_z \bar{I}_z} \delta(\xi - \xi_1) d\xi_1 \right\}$$

$$R_k(\xi, 0, 0, \tau) = \frac{1}{8\pi^3} \frac{\partial^2}{\partial \xi^2} \frac{R(\xi, \tau)}{\bar{I}_z \bar{I}_y} . \quad (21)$$